Supplemental Material Table of contents

Supplementary Methods

db/db mice

db/db mice on C57BLKS/J genetic background (including 71% C57BL/6J and 25% DBA/2J; no. 000642, Jackson Laboratories) were used as diabetic models, and db/+ mice on C57BLKS/J genetic background (no. 000642, Jackson Laboratories) were used as non-diabetic controls. For additional studies, PT-Pck1CKO (γGT^{cre}/$Pck1^{flox/flox}$) mice, which we generated on C57BL/6J genetic background, were first backcrossed to C57BLKS/J mice (no. 000662, Jackson Laboratories) for 4 generations before being crossed to db/+ mice to generate db/db PT-Pck1 CKO mice. Littermate db/db $Pck1^{flox/flox}$ mice were used as diabetic controls, and littermate db/+ PT-Pck1 CKO, as well as db/+ Pck1flox/flox mice, were used as non-diabetic controls. All of the mice used in the experiments were males and housed individually at 23 °C on a 12:12-hour light-dark cycle, with free access to food and water. The following 4 genotypes were used: *1*) Control (Cont)-non-diabetic (ND), *2*) Cont-*db/db*, *3*) CKO-ND, and *4*) CKO-*db/db*. At age of 8, 16, and 32 weeks, mice were sacrificed (Supplementary Fig.1-4, S-Fig1-4).

Histopathological examination

Mice kidney tissue was fixed in 10% neutral-buffered formaldehyde, embedded in paraffin, and cut into 4-μm thick sections. Immunohistochemistry was performed as described in the Method section. In brief, 4-μm-thick paraffin sections were fixed in 3% formaldehyde and stained with primary antibodies against TIMP-1(Abcam, Cambridge, MA, USA). These sections were stained with biotin-labeled goat antirabbit immunoglobulin G (IgG) (Vector Laboratories, UK) or biotin-labeled anti-mouse IgG

(Vector) and then treated with the Vectastain Elite ABC Kit (Vector). Each image of the stained sections was scanned using a 3CCD camera (Olympus Optical, Tokyo, Japan). To investigate the localization of STZ-induced or Pck1 defect-induced apoptosis, we performed double immunofluorescence staining of TUNEL and a PT-marker; AQP-1 in the kidney as described previously.[1]

RNA isolation, reverse transcription, and quantitative polymerase chain reaction (PCR)

Total RNA was extracted from culture cells and tissues using the RNeasy Plus Mini Kit (QIAGEN, Hilden, Germany). Real-time PCR was conducted using the ABI Prism 7700 Sequence Detection System (Applied Biosystems, Foster City, CA, USA) and SYBR GREEN System (Applied Biosystems). Each gene's relative mRNA levels were normalized to the level of mRNA expression for the housekeeping gene, *GAPDH*. The following primers were used: *Megalin*, F(5′-TGACTGCGGAGACATGAGTG-3′) and R(5′-CACAGACCCAGTGTTGTGGA-3′); *Cubilin*, F(5′-ATTTTCTCTGGGGTTTTGTTAC-3′) and R(5′-TAAGTTTCCCTCCTCCGTAG-3′); *Amnionless*, F(5′-CCATCTCGGATATGCTCCTG-3′) and R(5′-TTACAAGCTGGGTCCGAGTC-3′); *TGF-βI* F(5′-TTCATGAACCCAAGGGCTACC-3′) and R(5′-CTGGTTGTACAGAGCCAGGAC-3′); *Type IV collagen* F(5′-GGACAAGCAGGCTTTCCTGGA-3′) and R(5′-TGCTGTCCAGGAAGGCCAGG-3′); *TIMP-1* F(5′-GCTTCTGGCATCCTGTTGTTG-3′) and R(5′-GTCCGTCCACAAGCAATGAGT-3′) and *GAPDH*, F(5′-CCAGGGCTGCTTTTAACTC-3′) and R(5′-GCTCCCCCCTGCAAATGA-3′).

Cell culture

TIMP-1's effect on ECM deposition was investigated using LLC-PK1 porcine renal epithelial cells (ATCC, Manassas, VA, MD, USA; lot number: 59681631). The culture cells were grown at 37°C and 5% CO_2, in Dulbecco's modified minimal essential medium supplemented with heat-inactivated 10% fetal bovine serum (Thermo Fisher Scientific, San Jose, CA, USA). LLC-PK1 cells from passages 8 to 30 were used.

Constructs and transfection

TIMP-1 cDNA was cloned from human kidney cDNA using the primers previously described.[2] The PCR product was subcloned into the mammalian expression vector, pcDNA3.1(+) (Invitrogen). The expression plasmid containing Timp-1 cDNA (pcDNA3.1-Timp-1) and the control plasmid (pcDNA3.1) were transfected into LLC-PK1 cells using Lipofectamine 2000 (Invitrogen). The cells were harvested 48 hours after transfection for RT-PCR assays.

Enzyme activities

Kidney mitochondria were isolated using differential centrifugation as described previously.[3] Enzyme activities of mitochondrial Complex I (CI), Complex II (CII), Complex III (CIII), Complex IV (CIV). and Complex V (CV) were measured at room temperature using a Beckman Coulter DU 530 Spectrophotometer (Beckman Coulter, Brea, CA) as described previously.[3] Citrate synthase activity was measured at 412 nm (e = 13.6 mM-1 cm-1). Rotenone-sensitive CI, malonate-sensitive CII, antimycin A-sensitive (AA) CIII, KCN-sensitive CIV, and oligomycin-sensitive CV activities were

investigated. All activity results are averages of 7 assays from each group of mice's pooled samples.

Electron microscopy

For electron microscopy (EM) evaluation, the kidney tissues were harvested and fixed overnight at 4°C with 2% paraformaldehyde and 2% glutaraldehyde (GA) in 0.1 M phosphate buffer (PB; pH 7.4). Following fixation, the samples were washed three times with 0.1 M PB for 30 min each before being post-fixed with 2% osmium tetroxide (OsO4) in 0.1 M PB at 4°C for 2 h. The fixed tissue blocks were embedded in Epon epoxy resin. The average number of podocyte foot processes was counted and divided by the glomerular basement membrane (GBM) Length (μm) to evaluate the densities of the foot processes as described previously.[4] Counts were taken from 105 micrographs of at least three glomeruli in each mouse. Using Image-Pro Plus 7.0J, the length and thickness of the GBM were measured.

Measurement of ECAR

The mitochondrial extracellular acidification rate (ECAR) was measured in primary proximal tubular cells using a Seahorse XF Glycolysis Stress Test Kit (#103020-100, Seahorse Bioscience) and the Seahorse XF-24 extracellular flux analyzer. Primary tubular cells were seeded with Seahorse XF Culture Microplates. The calibration cartridge was hydrated at 37°C in a non-CO_2-containing incubator 1 day before the assay. The growth medium was replaced with Seahorse XF Base Medium (#103193-100, Seahorse Bioscience) containing glutamine (1 mM) and the cells were incubated at 37°C in a non-CO_2-containing incubator for 1 hour. To calculate the ECAR, three

reagents were used: glucose (10 mM), oligomycin (1 μM), and 2-deoxyglucose (50 mM).

Immunoblotting

Immunoblotting was performed using specific antibodies against MRPL13 (Abcam), MRPS15 (Abcam), VDAC1 (Abcam), and Lamin B1 (Abcam). The loading control was the GAPDH band, which was recognized by a specific antibody (Sigma-Aldrich). Band intensities were calculated using the Scion Image Software (Scion Corp, Frederick, MD, USA).

Supplementary Results

Changes in albumin reabsorption-related molecules in CKO and TG mice

We conducted RT-PCR analysis to identify the changes in albumin reuptake-related molecules like megalin, cubilin, and aminonless (S-Fig5). In CKO (S-Fig. 5A) or WT+STZ mice (S-Fig. 5B), these molecules were significantly lowered, which was retained in TG+STZ mice. TGF-β reportedly lowered megalin and cubilin in proximal tubules.[7] In CKO or WT+STZ mice, TGF-β levels were increased. In contrast, these levels were lowered in TG+STZ mice. Therefore, according to previous reports[5], TGF-β levels might be critical in downregulating megalin, cubilin, and aminonless in our mice.

TIMP-1 contributes to the elevation of ECM deposition in CKO

We evaluated the upstream regulator of TGF-β and type IV collagen. Tissue inhibitor metalloproteinase-1 (TIMP-1) is recognized as a pro-fibrogenic gene to upregulate TGF-β and type IV collagen.[6] We thus assessed the TIMP-1 levels by performing immunostaining (S-Fig 6A). It demonstrated that the TIMP-1 expression was markedly higher in CKO and WT+STZ mice than in control mice or WT mice. To verify the effect of TIMP-1 on proximal tubular TGF-β and type-IV collagen production, we constructed TIMP-1 overexpression vectors (S-Fig 6B) and discovered that TIMP-1 overexpression rose the levels of both type-IV collagen and TGF-β1 (S-Fig 6B) by transfecting them into LLCPK-1 cells**.** As mentioned in the following, mitoribosomal dysfunction resulted in the production of ROS such as superoxide, which reportedly increases TIMP-1 levels.[7] Therefore, mitoribosomal dysfunction increases ROS, resulting in increased TIMP-1 levels and renal fibrosis.

Impairment of OXPHOS complex activity in CKO

To assess the mechanisms where mitROS was elevated in CKO (Fig. 4F) or WT+STZ mice (Fig. 8F), we measured the activity of OXPHOS complexes (S-Fig7). Previous research claimed that mitochondrial ETC dysfunction in OXHPOS systems caused electron leakage reacting with O^2, resulting in superoxide production.[8, 9] CKO or WT+STZ exhibited markedly reduced activities, as normalized to citrate synthase activity, of complexes I, III, IV, and V but not complex II. Major component proteins of complex I, III, and IV were synthesized in mitoribosomes, and the synthesis of complex II-related proteins was synthesized in cytoplasmic ribosomes. Therefore, the mitoribosome defect in CKO or WT+STZ reduced the activity of complex I, III, IV, and V. Previous reports also found that the dysfunction of complex I[10] and/or III[11] caused the increase in mitROS such as superoxide, which is consistent with our results.

Glomerular phenotypes of CKO and TG mice

In terms of the EM findings, we evaluated the thickness of the GBM and the density of the foot process of the podocytes (S-Fig 8**)**. The GBM thickness or the foot process density did not vary between Cont and CKO. In contrast, GBM thickening and foot process effacement was elevated in WT+STZ, which was also found in TG+STZ. Therefore, the mechanism by which albuminuria levels were lower in TG+STZ was thought to be the mitigation of proximal tubular damages in TG+STZ mice caused by the protection of mitoribosome functions and its' concomitant retaining the function of albumin reabsorption.

ECAR in CKO and TG mice

We assessed the glycolysis levels by conducting ECAR assays using primary tubular cells harvested by each group of mice (S-Fig 9). Cells harvested from Cont or WT+Sal responded to blocked mitochondrial respiration (treatment with oligomycin) by raising their glycolytic flux. By contrast, Pck1-lacking cells harvested from CKO or WT+STZ demonstrated a high level of glycolysis already at baseline that did not increase after blocking OXPHOS. These outcomes indicate that cells without Pck1 rely on glycolysis rather than OXPHOS for energy generation, because of their inability to sustain sufficient energy generation by OXPHOS.

Supplementary Figure Legends

Supplementary Figure 1.

Effects of *Pck1* CKO on urinary albuminuria in db/db mice

(A) A schematic illustration showing the experimental schedule of db/db mice. (B) Temporary changes in the protein expression of *Pck1* in db/db mice. Representative images of kidney cryosections obtained from db/db mice were stained by immunofluorescence for *Pck1* (green) and costained for AQP1 (red), a proximal tubule marker. Scale bar, 50 μm; N = 3. (C) Schematic showing the 4 groups of mice used in the following research. (D) Pck1 immunofluorescence intensity levels in each group of mice. Kidney tissue specimens obtained from each mouse at 32 weeks of age were stained using immunofluorescence for *Pck1* (green) and AQP1 (red). The right panel represents the quantitative analysis of the *Pck1* fluorescence intensity. Scale bar, 50 μm; N = 3. (E) Temporal changes in the mean plasma glucose concentrations in the mice of each group. We assessed the mice at 8, 16, 24, and 32 weeks of age, respectively. N = 7 mice per group. (F) Body weight changes from 8 to 32 weeks of age in each mouse. N = 7 mice per group. N = 7. Statistically significant differences in each group are denoted by horizontal bars. *$p < 0.05$.

Supplementary Figure 2.

Renal phenotypes in proximal tubule-specific *Pck1* CKO-db/db mice

(A) Serum creatine levels in each mouse at 32 weeks of age. N = 7 per mice group. (B) Urinary albumin excretion in each mouse at 32 weeks of age. N = 7 per mice group. (C) SDS-PAGE of mouse urine samples. Urine samples of 32-week-old each group of mice was tested with a 15% SDS-PAGE before staining with Coomassie blue. N = 2 mice per

group. (D) Representative pictures of albumin staining in each mouse. Arrows denote albumin cast in CKO-ND mice. The right panel shows the relative staining intensity. N = 7 mice per group. (E) Apoptotic tubular cells in the 4 groups of mice. Arrows denote apoptotic cells. The bar graph shows the quantitative analysis of apoptotic tubular cells. N = 7 mice per group. (F) Representative photomicrographs showing TGF-β immunostaining in each group. The bar graph represents the quantitative analysis of TGF-β staining. N = 7 per mice group. (G) Representative photomicrographs indicate collagen IV immunostaining in each group. The bar graph shows the quantitative analysis of collagen IV stainings. N = 7 per mice group. (D, E, F, and G) Light micrograph; scale bar = 100 μm. Kidney tissue specimens for immunostaining were derived from the 4 groups of mice at 32 weeks of age. All data are depicted as mean ± standard error of the mean. Statistically significant differences in each group are indicated by horizontal bars. *$p < 0.05$.

Supplementary Figure 3.

HK2 expression in Pck1 CKO-db/db

(A) Representative images of sections immune-stained with HK2 in the kidneys from each mouse at 32 weeks of age. Scale bar, 50 μm. The right panel indicates proportional staining areas for HK2. N = 7. Statistically significant differences in each group are indicated by horizontal bars. *p < 0.05. (B) Presumed regulatory mechanisms for HK2 expression in db/db mice. (C) Presumed regulatory mechanisms for HK2 expression in CKO-db/db mice.

Supplementary Figure 4. Mitoribosomal phenotypes in *Pck1* CKO-db/db

(A) Representative electron micrograph in each group. Scale bar = 500 nm. Blue squares imply enlarged regions. (B) Expanded images of Supplementary Figure 4A are presented. Blue arrowheads denote mitoribosomes. Scale bar = 500 nm. (C) Real-time quantitative reverse transcription analysis of renal mRNA levels of mitoribosome markers such as MRPL13 and MRPS15. (D) Illustration denoting the mitoribosomal defect in CKO-ND mice and the mitoribosomal proliferation in Cont-db/db and CKO-db/db mice. For EM, the kidney tissue specimens were incorporated in Epon epoxy resin. Electron micrographs of 10 PTs per kidney were randomly derived for each mouse to evaluate the morphometry of the PTs.

Supplementary Figure 5. Changes in albumin uptake-related molecules in *Pck1* CKO and TG

(A) The kidney tissue specimens for RT-PCR were derived from CKO and control mice at 32 weeks of age. N = 6 mice per group. (B) The kidney tissue specimens for RT-PCR were derived from each experimental group: WT (wild-type mice)+Sal (saline), WT+STZ, TG+Sal, and TG+STZ mice at 32 weeks of age. N = 6 mice per group. Real-time quantitative reverse transcription analysis of renal mRNA levels of megalin, cubilin, and amnionless. Glyceraldehyde 3-phosphate dehydrogenase was a control. All data are depicted as the mean ± standard error of the mean. Horizontal bars denote statistically significant differences between groups. *$P < 0.05$.

Supplementary Figure 6. The role of TIMP-1 in diabetic fibrotic changes in Pck1 deficiency

(A) Representative photomicrographs demonstrating TIMP-1 immunostaining in each group of mice at 32 weeks of age. The bar graph depicts the quantitative analysis of TIMP-1 staining. N = 7 per mice group. Scale bar, 50 μm. (B) The impacts of TIMP-1 overexpression on type-IV collagen and TGF-β1 expression in LLCPK-1 cells. After LLCPK-1 cells were transfected with pcDNA3.1 or empty vectors, the cells with no transfected control cells (Cont) were subject to RT-PCR used with TIMP-1 (Left), type-IV collagen (Middle), or TGF-β1 (Right) -specific primers. The bar graph in the lower panels depicts the quantification of the band intensity. Statistically significant differences in each group are indicated by horizontal bars. *$p < 0.05$.

Supplementary Figure 7 Measurement of mitochondrial ETC complex enzyme activities in the kidneys of CKO and TG mice.

Complex activities were analyzed as described in Methods. All activity findings are the average of 7 assays from the pooled samples of each group of mice at 32 weeks of age. Citrate synthase activities were used to normalize mitochondrial proteins. Activities for CI-CV are plotted. All data are shown as the mean ± standard error of the mean. Horizontal bars imply statistically significant differences between groups. *$P < 0.05$. (A) The kidney tissue specimens were obtained from CKO and control mice at 32 weeks of age. (B) The kidney tissue specimens were derived from each experimental group: WT+Sal, WT+STZ, TG+Sal, and TG+STZ mice at 32 weeks of age.

Supplementary Figure 8. Glomerular histological changes in CKO and TG mice.

Representative EM images of GBM in each group of mice. The GBM and foot processes are depicted (scale bar, 1 μm). Graph showing the GBM thickness from 20

measurements per group. Graph showing the density of the foot process per micron of GBM from 20 measurements per group. All data are shown as mean ± standard error of the mean. Statistical significance between each group is indicated by a horizontal bar. *$P < 0.05$. (A) The kidney tissue specimens were derived from CKO and control mice at 32 weeks of age. (B) The kidney tissue specimens were derived from each experimental group: WT+Sal, WT+STZ, TG+Sal, and TG+STZ mice at 32 weeks of age.

Supplementary Figure 9. Glycolysis assay in CKO and TG mice.
Glycolysis assay of ECAR in primary renal tubular cells isolated from the kidneys of each group of mice (n = 3 independent experiments). Three chemical reagents were included: glucose (10 mM), oligomycin (1 μM), and 2-deoxyglucose (50 mM). Data are mean ± SEM and were assessed using Student's t-test (*p < 0.05 versus WT+Sal or Cont). (A) The kidney tissue specimens were obtained from CKO and control mice at 32 weeks of age. (B) The kidney tissue specimens were taken from each experimental group: WT+Sal, WT+STZ, TG+Sal, and TG+STZ mice at 32 weeks of age.

Supplementary Figure 10-15. Apoptotic cells in proximal tubules of CKO and TG mice. Representative immunofluorescence double staining of TUNEL (green) and AQP1 (red, proximal tubules) in kidney tissues (n = 5). Scale bars, 50 μm. The kidney tissue specimens were derived from Cont (Supplementary Figure 10) and CKO mice (Supplementary Figure 11) at 32 weeks of age. The kidney tissue specimens were derived from each experimental group: WT+Sal (Supplementary Figure 12), TG+Sal (Supplementary Figure 13), WT+STZ (Supplementary Figure 14), and TG+STZ mice

(Supplementary Figure 15) at 32 weeks of age. White arrows denote apoptotic tubular cells.

Supplementary Figure 16. Reduced mitoribosomes in CKO mice

Western blot analysis of renal protein levels of intracellular organelle markers. MRPL13 and MRPS15 are mitoribosome proteins, while VDAC is a mitochondrial protein and Lamin B is a nuclear protein. The kidney tissue specimens were obtained from CKO and control mice at 32 weeks of age. The results of one representative experiment of the three performed are shown. All data are indicated as the mean ± standard error of the mean. Horizontal bars denote statistically significant differences between groups. $*P < 0.05$.

Supplementary Figure 17. Reduced mitoribosomes in WT+STZ mice

Western blot analysis of renal protein levels of intracellular organelle markers. MRPL13 and MRPS15 are mitoribosome proteins, while VDAC is a mitochondrial protein and Lamin B is a nuclear protein. The kidney tissue specimens were taken from each experimental group: WT+Sal, WT+STZ, TG+Sal, and TG+STZ mice at 32 weeks of age. The outcomes of one representative experiment of the three conducted are shown. All data are denoted as the mean ± standard error of the mean. Horizontal bars denote statistically significant differences between groups. $*P < 0.05$.

Supplementary Figure 18-27. Uncropped blots of Supplementary Fig16-17.

Uncropped Western Blots images were shown.

Supplemental Figure 28 Gene map depicting mit-DNA-encoded genes.

These genes are translated in mitoribosomes to produce each protein.

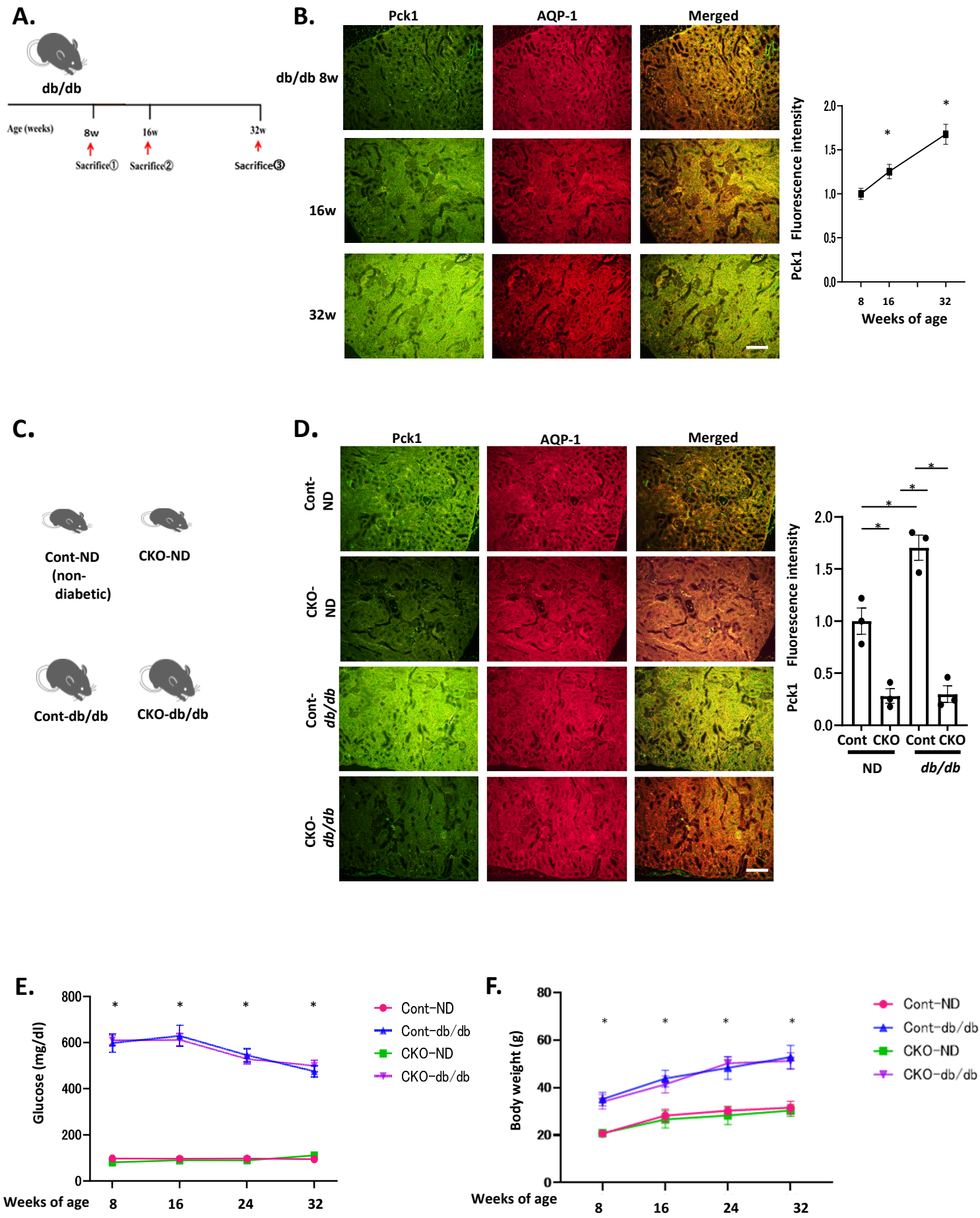

Supplementary Figure 1, Hasegawa et al.

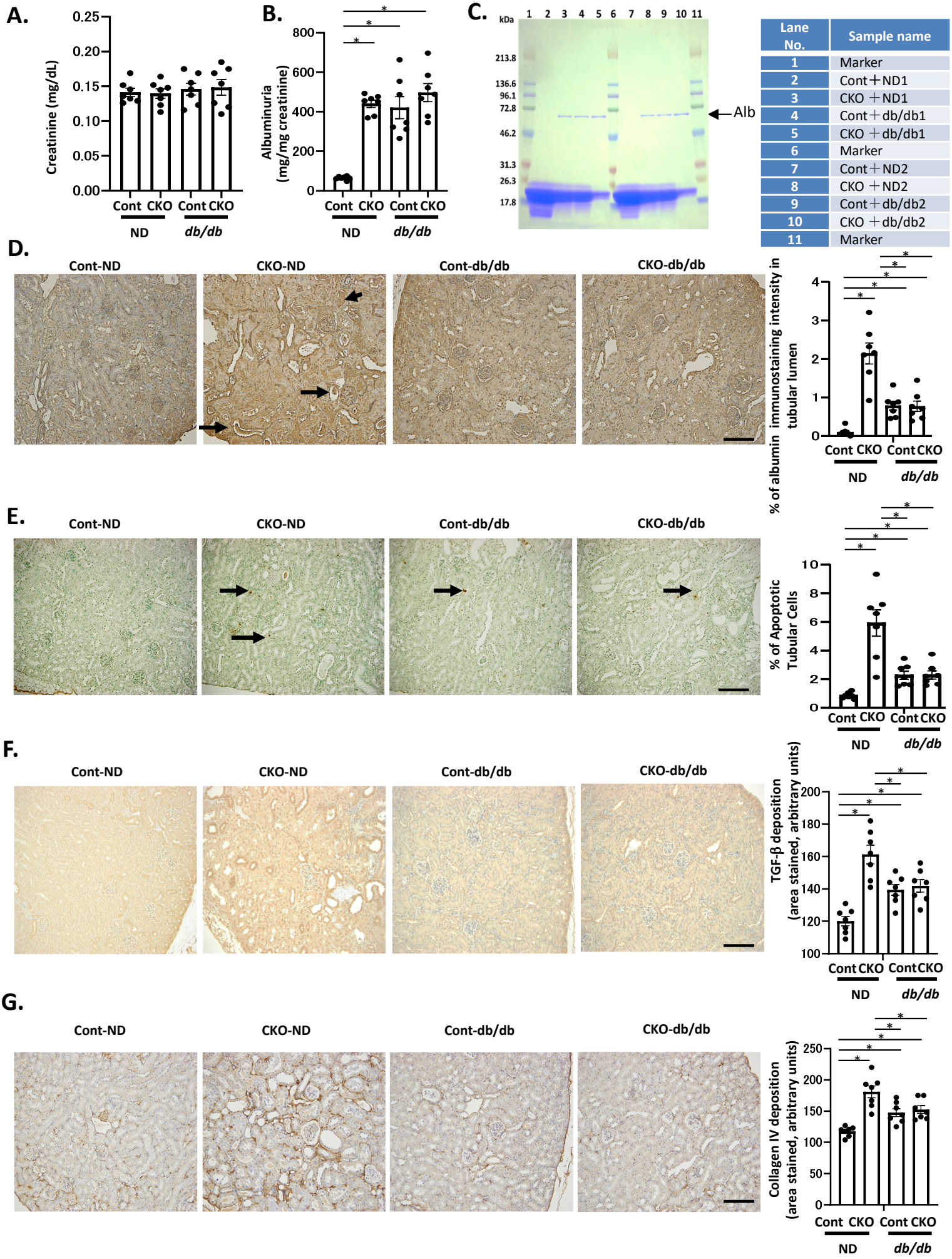

Supplementary Figure 2, Hasegawa et al.

A.

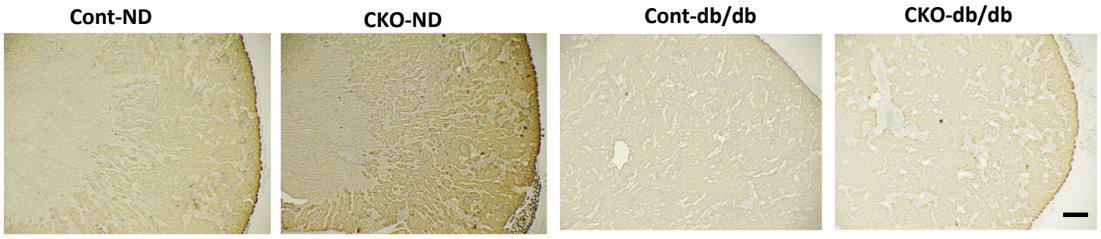

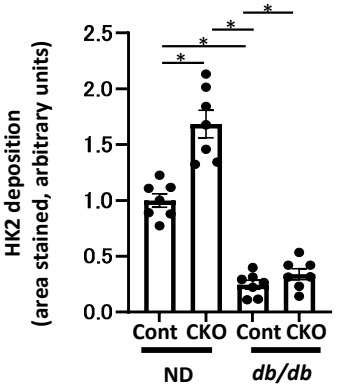

B.

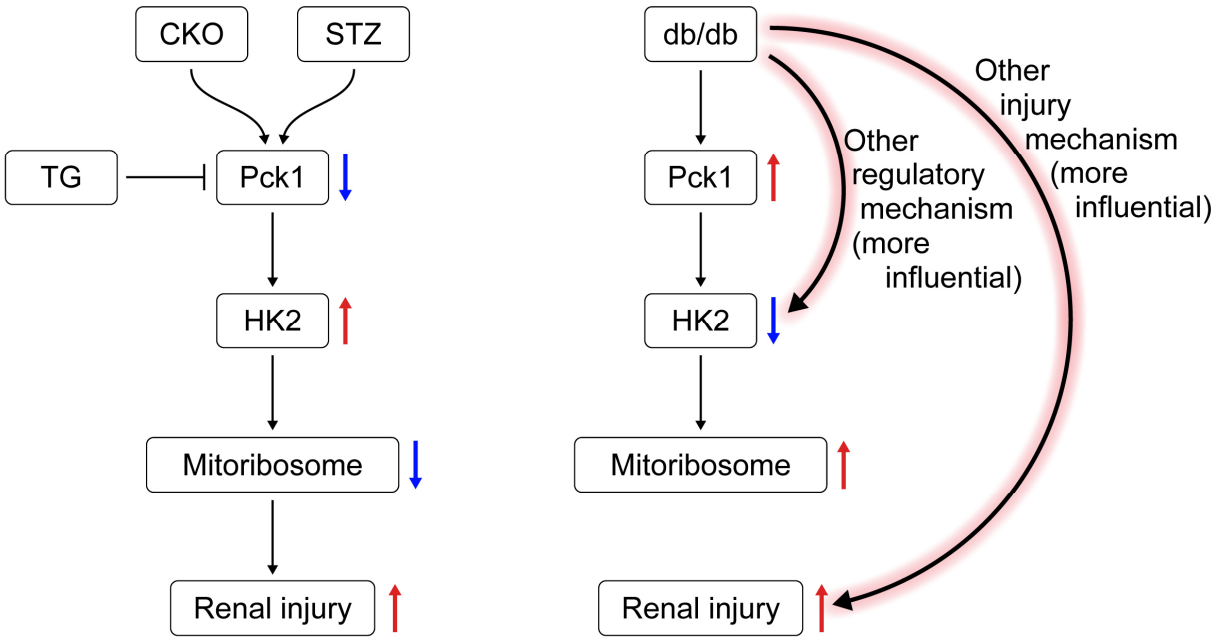

C.

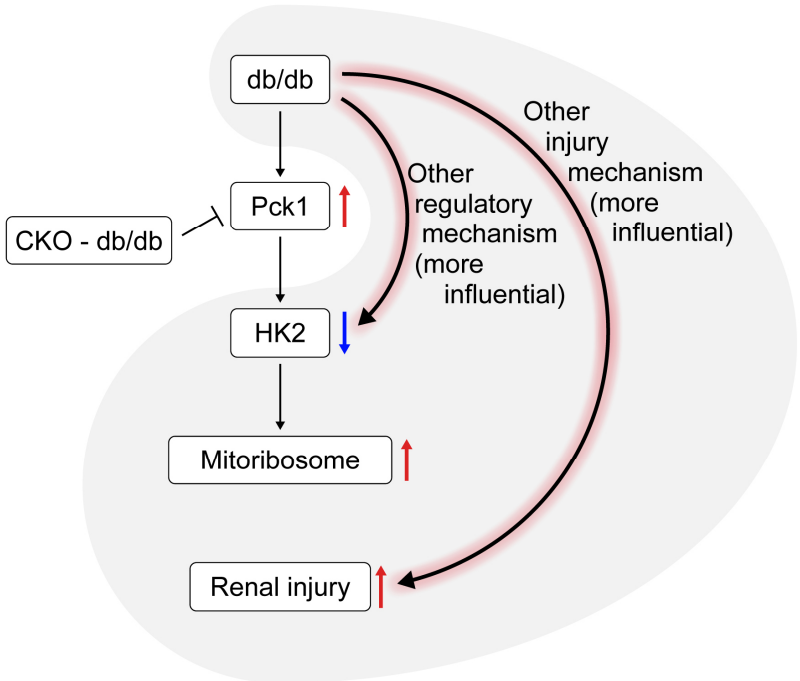

Supplementary Figure 3, Hasegawa et al.

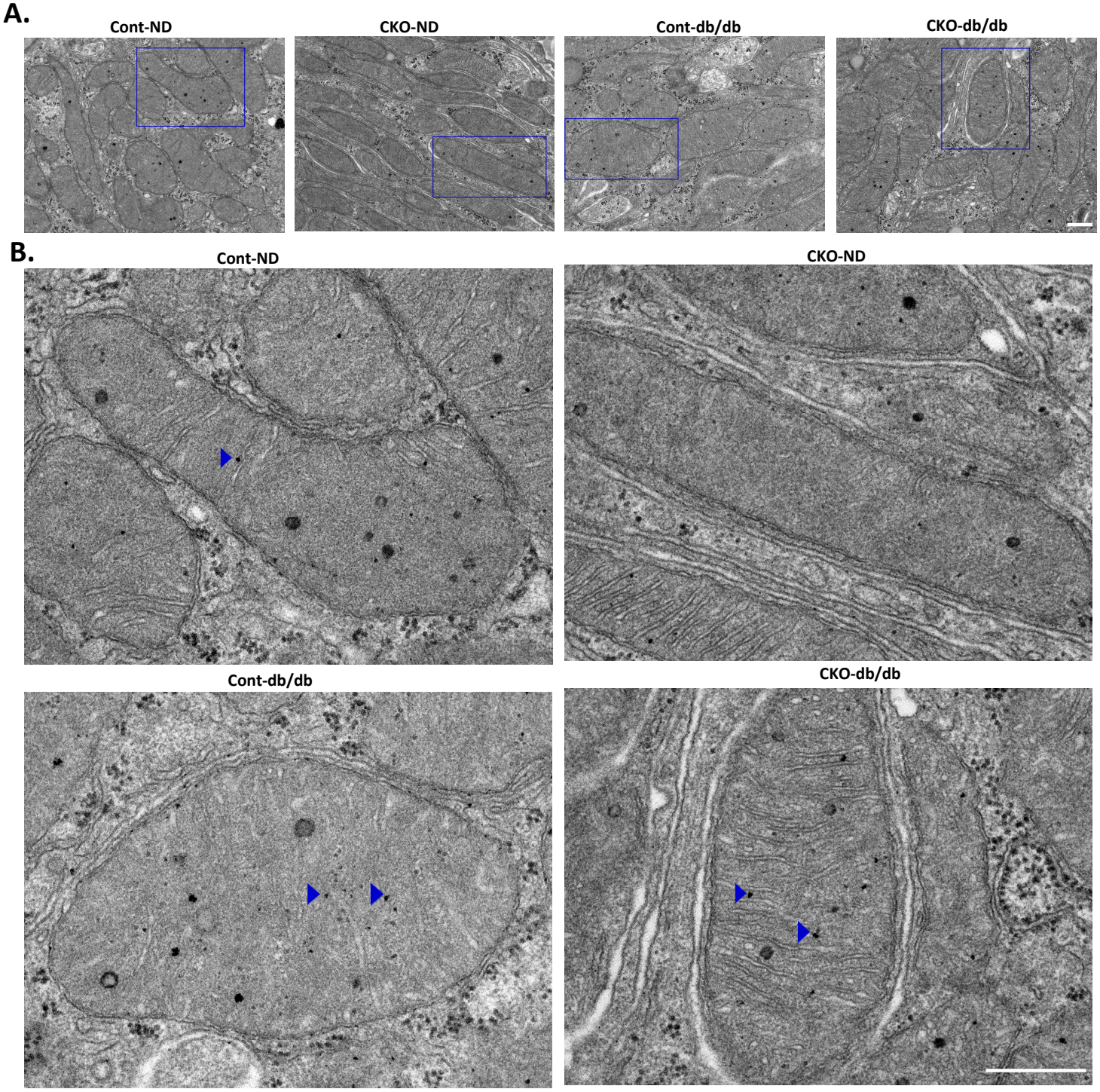

Supplementary Figure 4, Hasegawa et al.

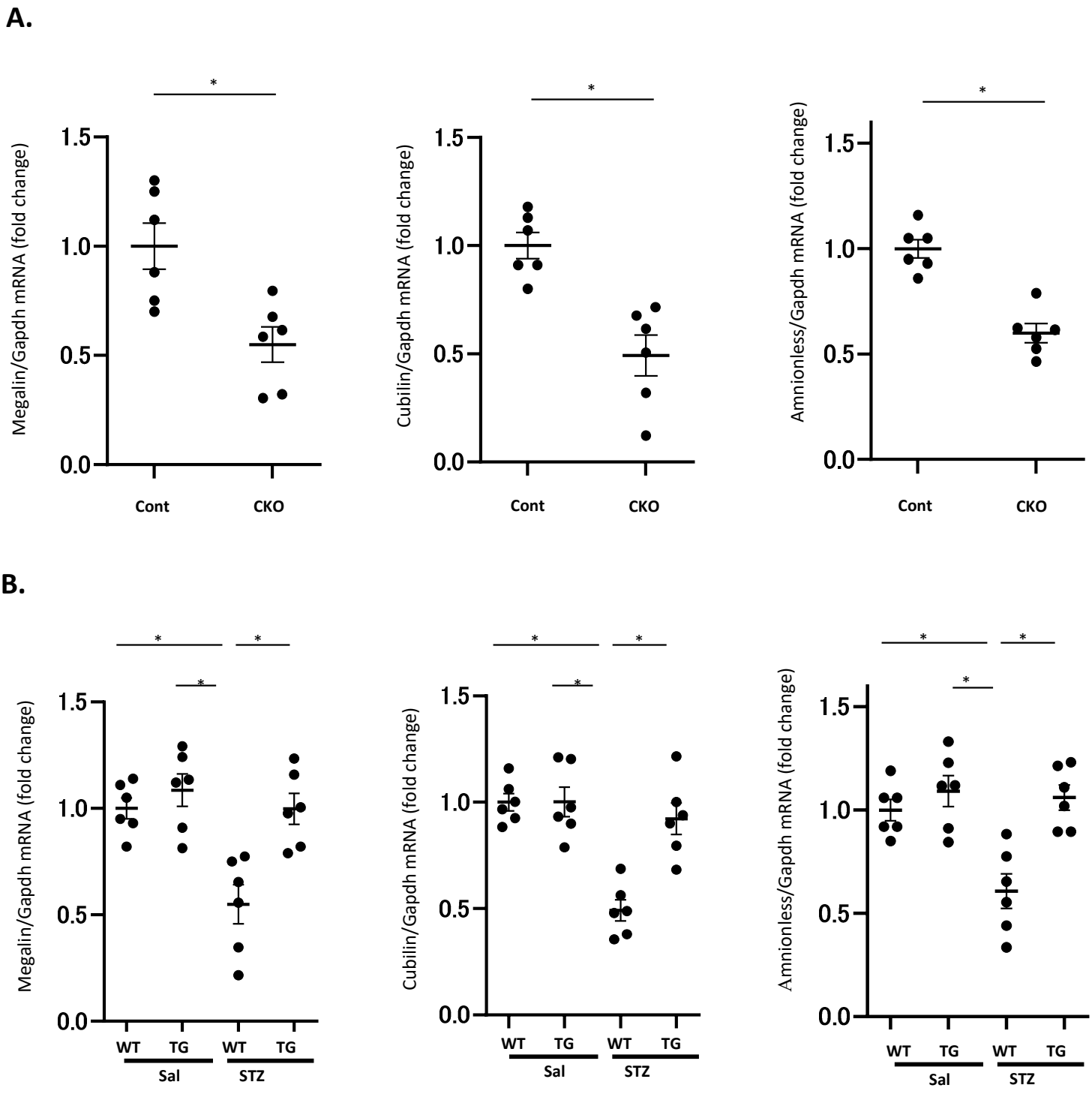

Supplementary Figure 5, Hasegawa et al.

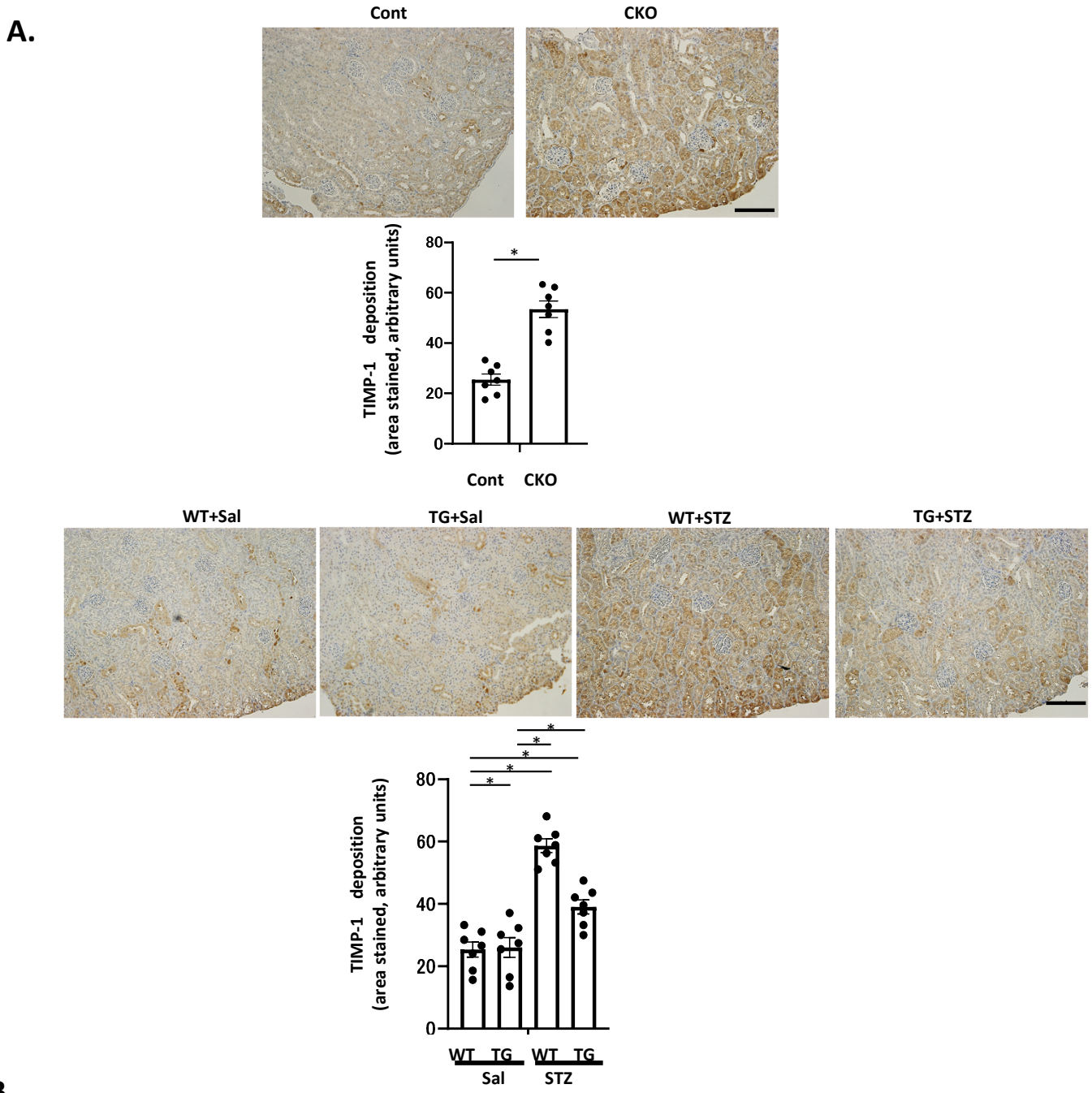

Supplementary Figure 6, Hasegawa et al.

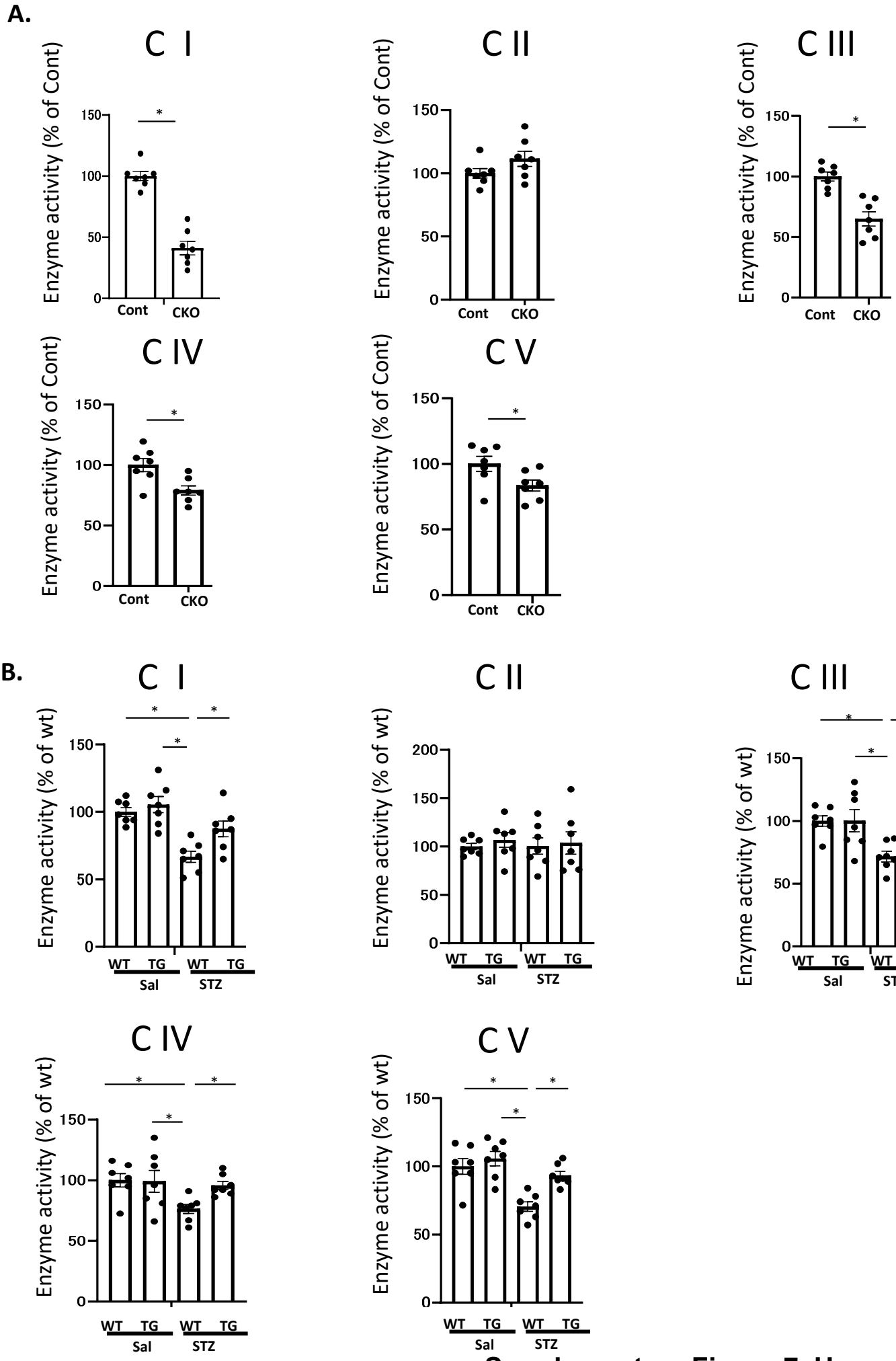

Supplementary Figure 7, Hasegawa et al.

A.

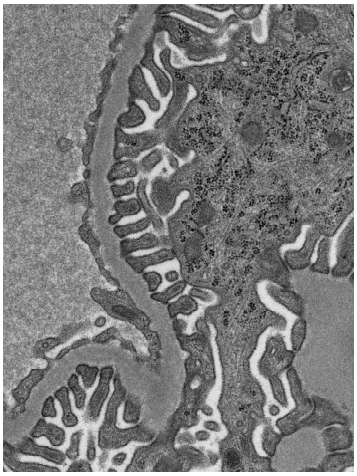

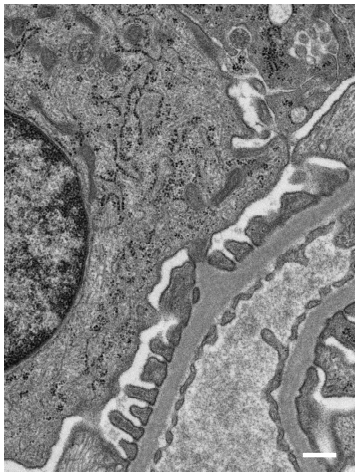

Cont

CKO

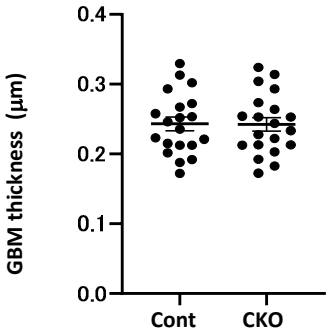

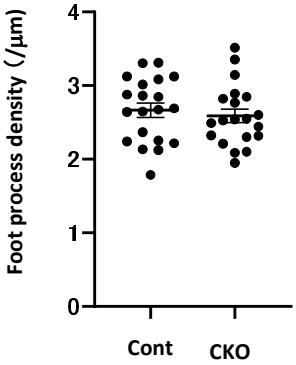

B.

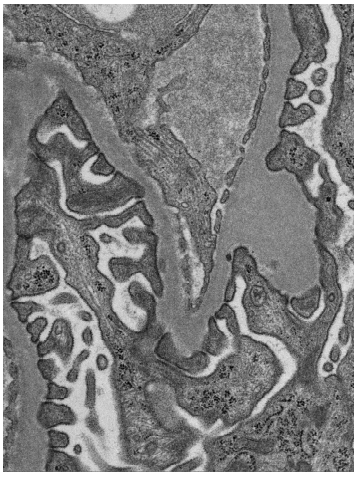

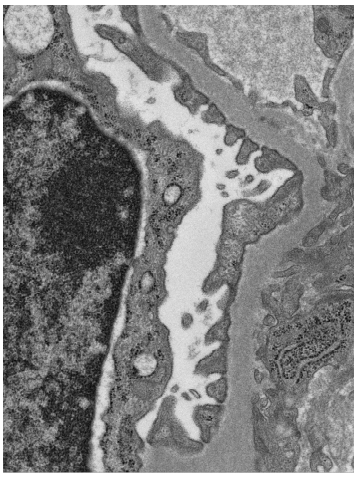

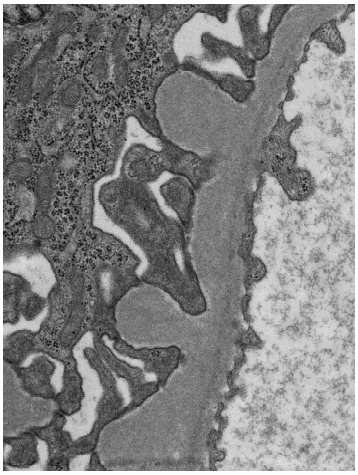

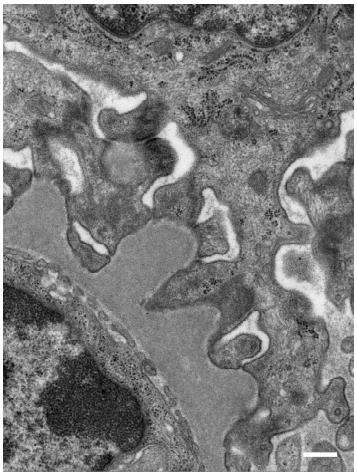

WT＋Sal

TG＋Sal

WT＋STZ

TG＋STZ

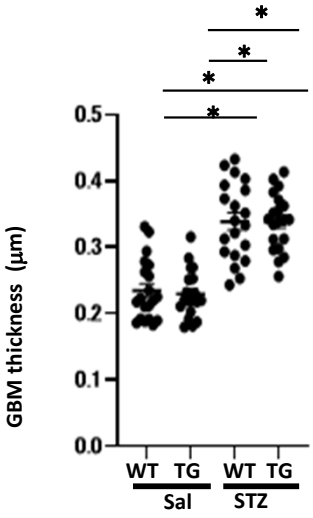

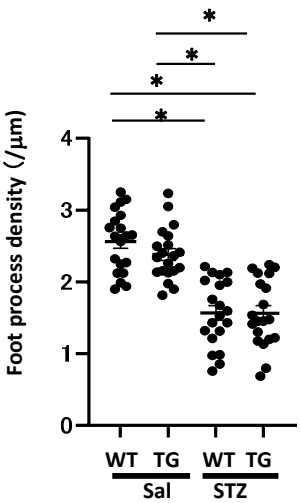

Supplementary Figure 8, Hasegawa et al.

ECAR

A.

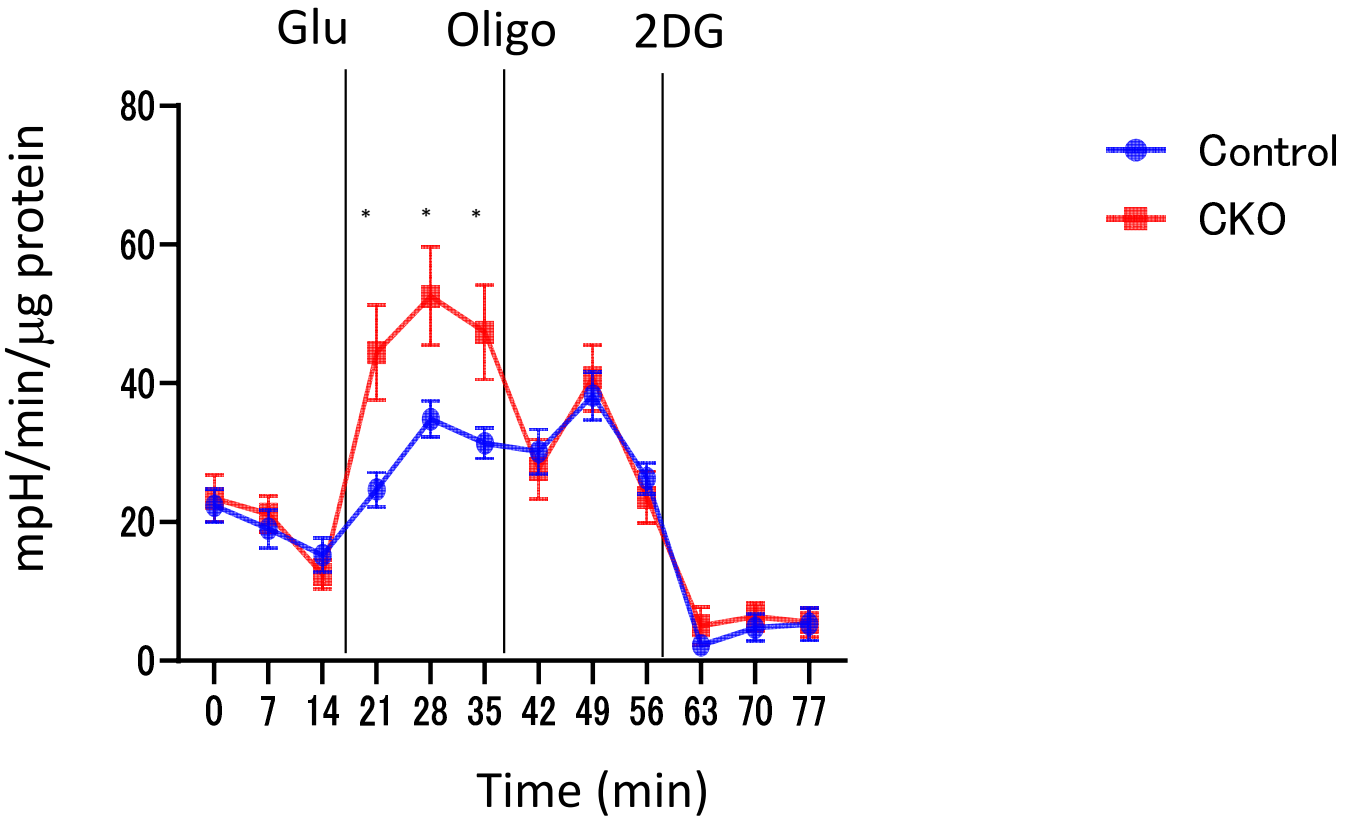

B.

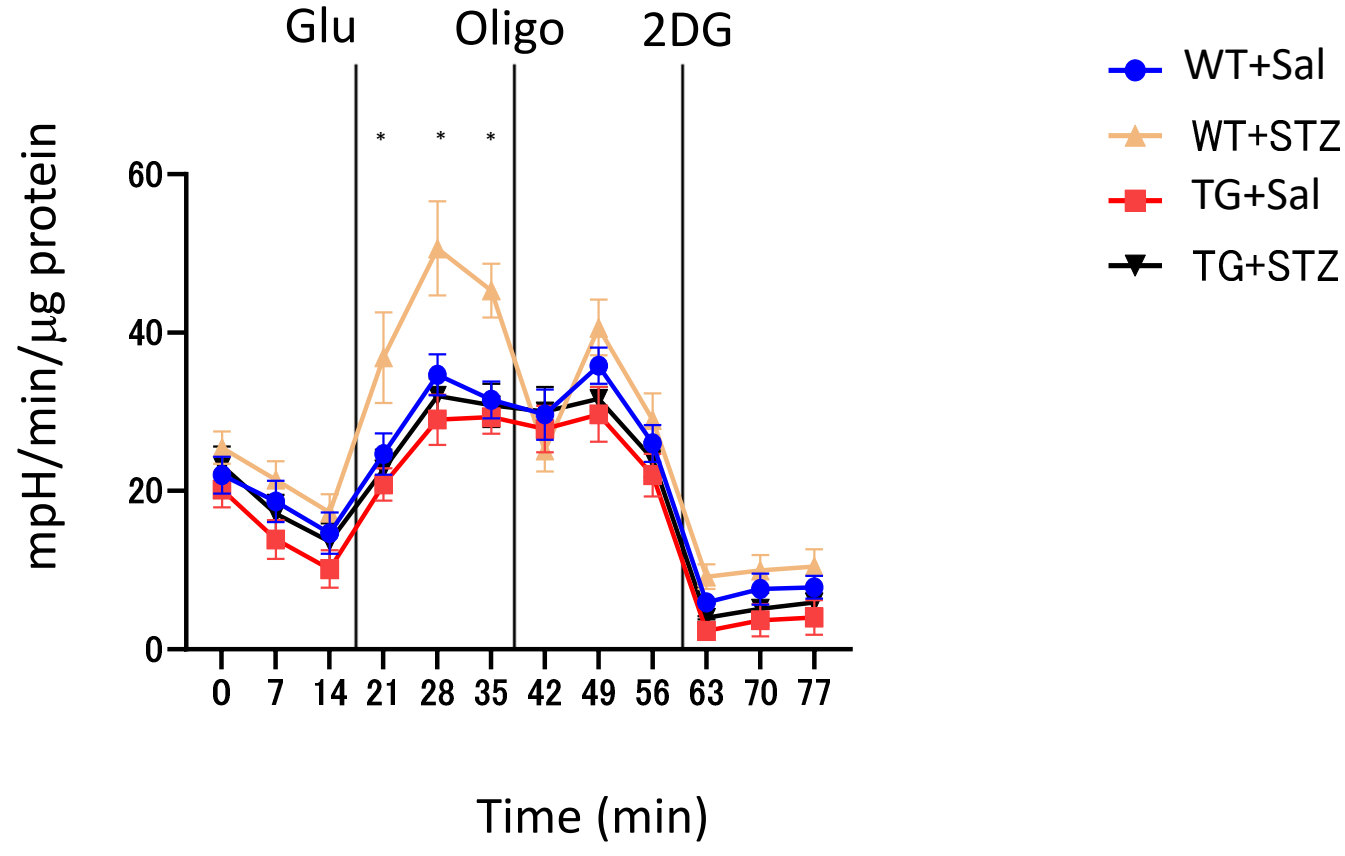

Supplementary Figure 9, Hasegawa et al.

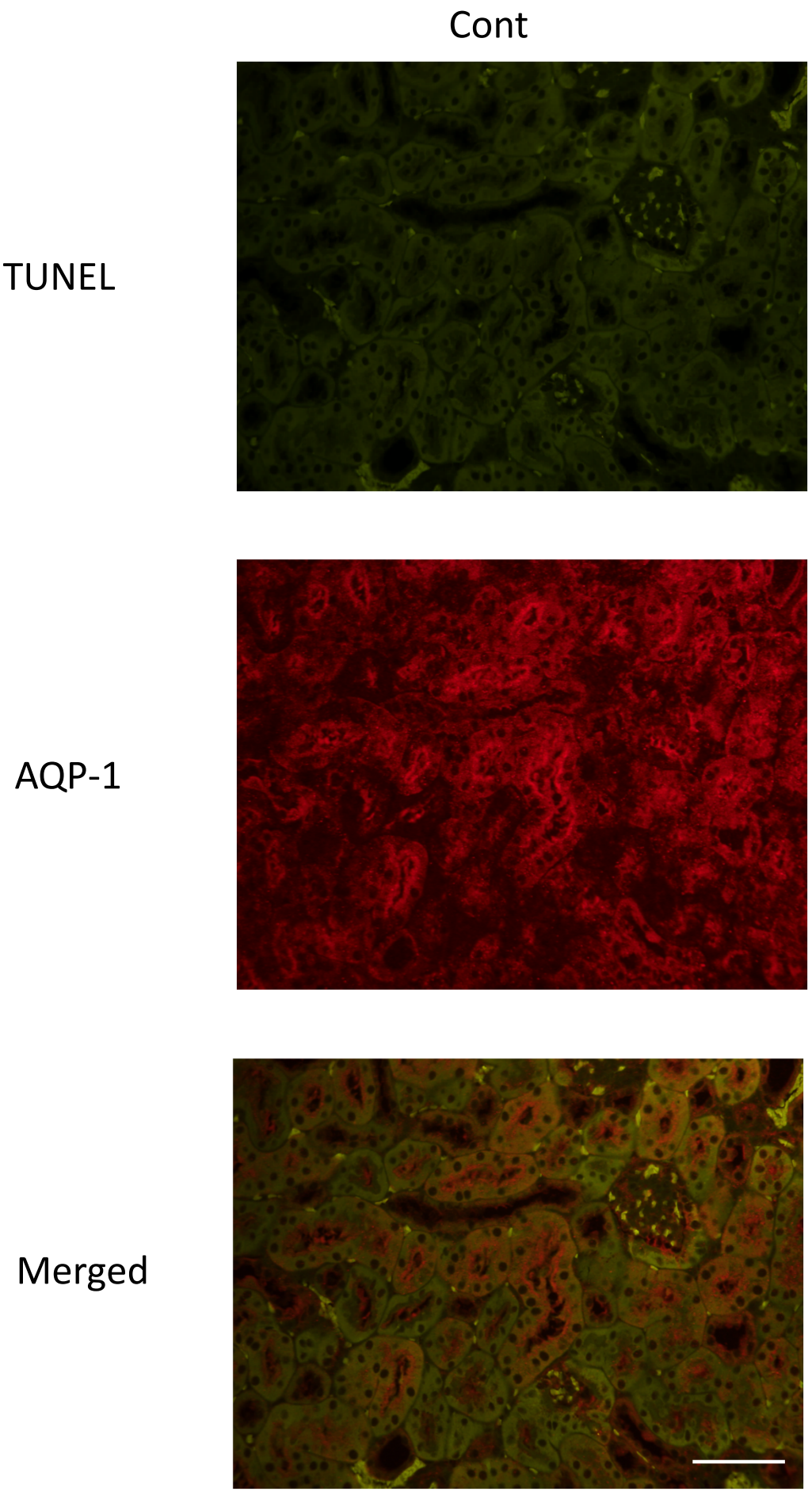

Supplementary Figure 10, Hasegawa et al.

CKO

TUNEL

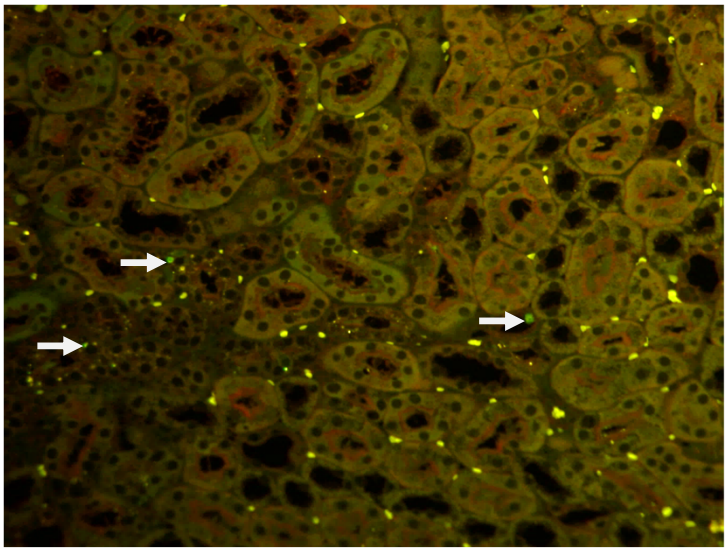

AQP-1

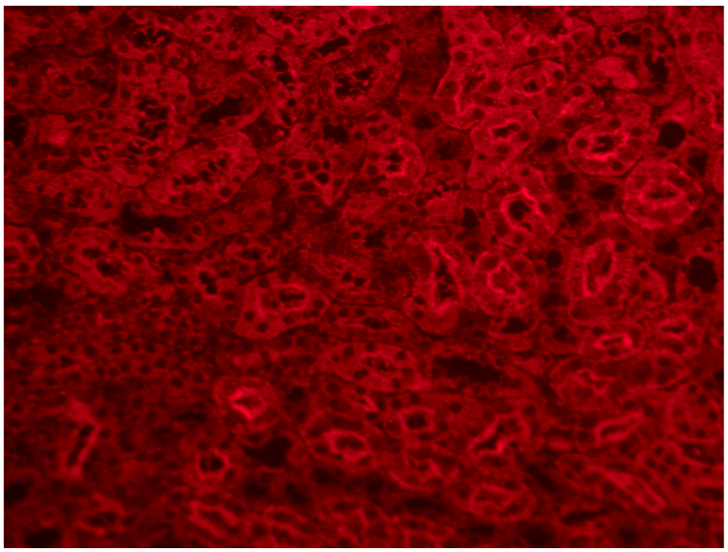

Merged

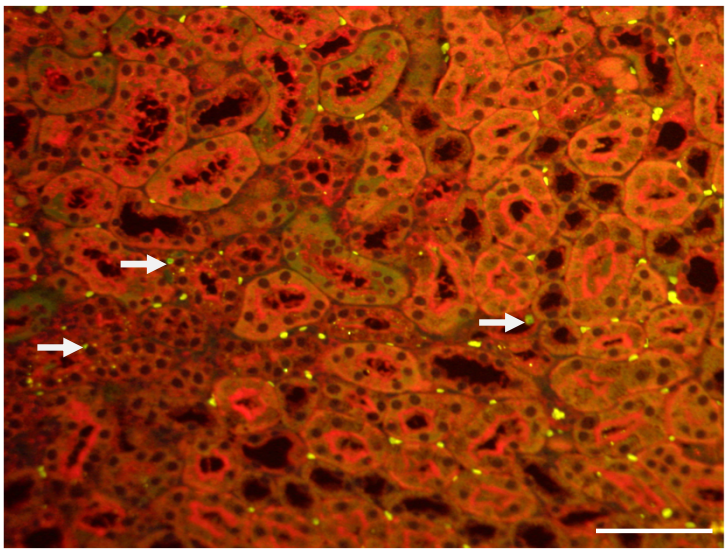

Supplementary Figure 11, Hasegawa et al.

WT+Sal

TUNEL

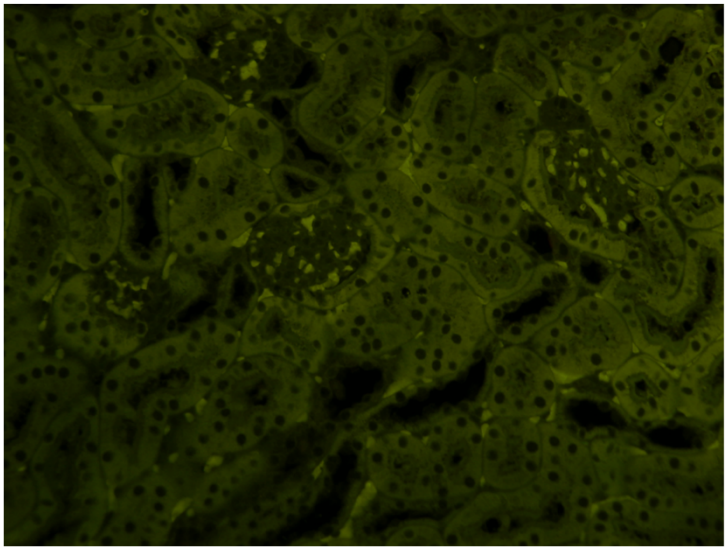

AQP-1

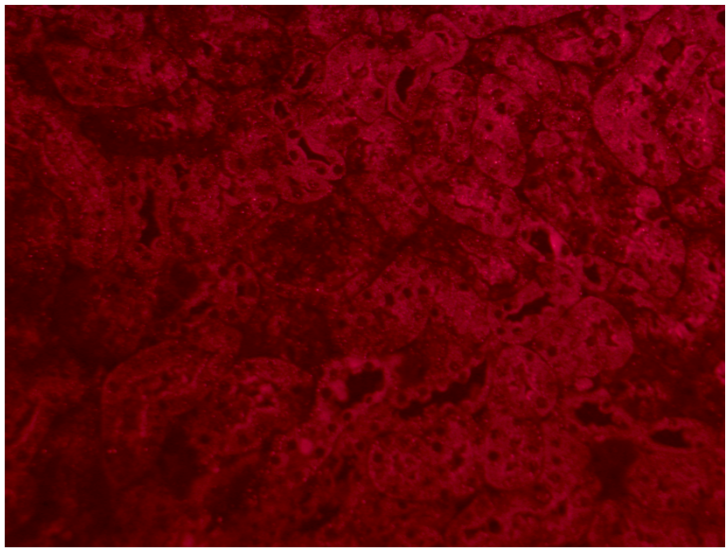

Merged

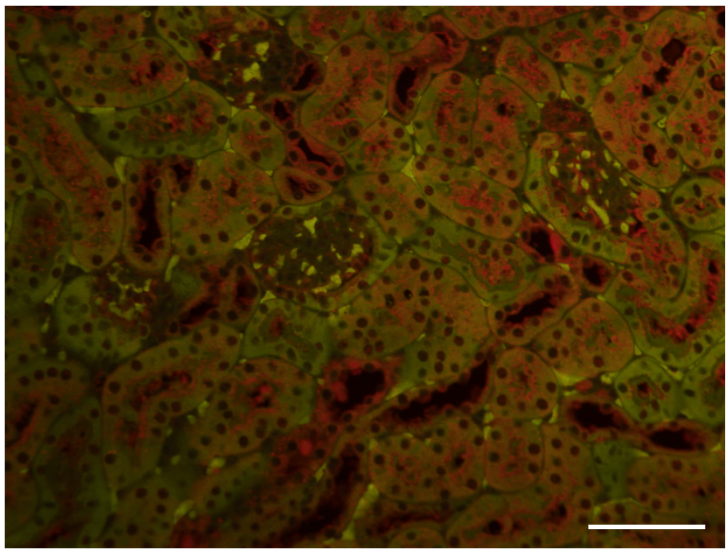

Supplementary Figure 12, Hasegawa et al.

TG+Sal

TUNEL

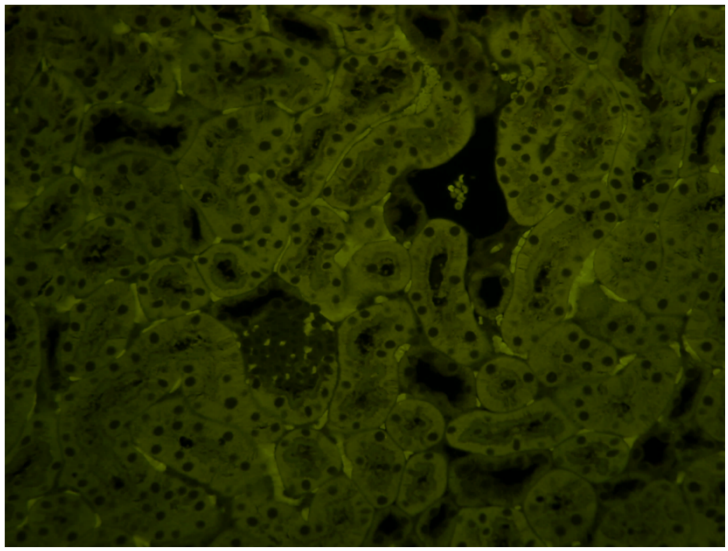

AQP-1

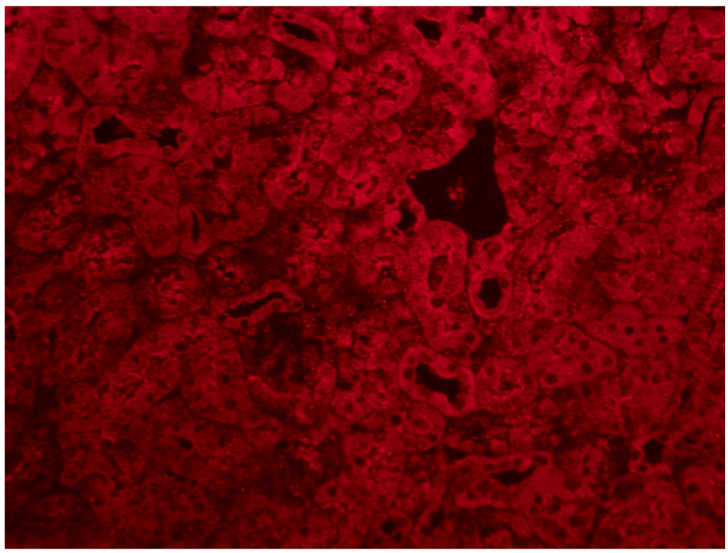

Merged

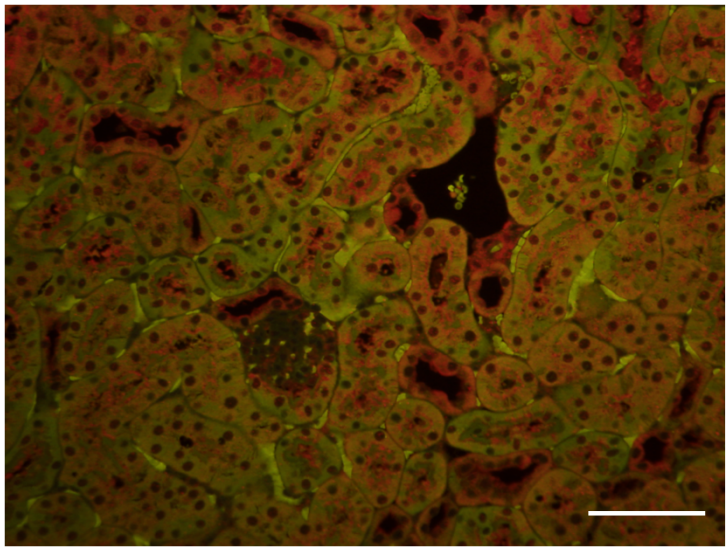

Supplementary Figure 13, Hasegawa et al.

WT+STZ

TUNEL

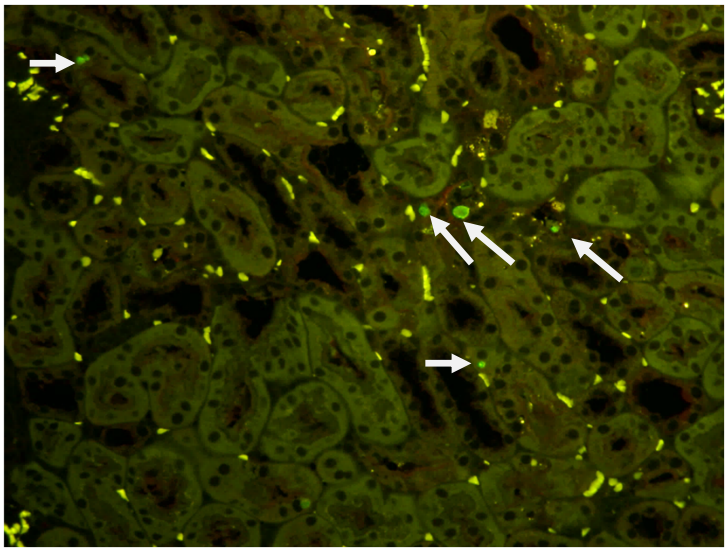

AQP-1

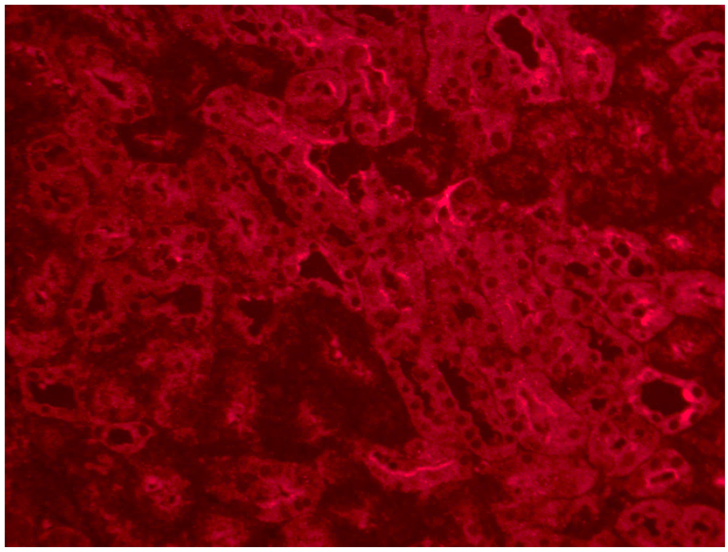

Merged

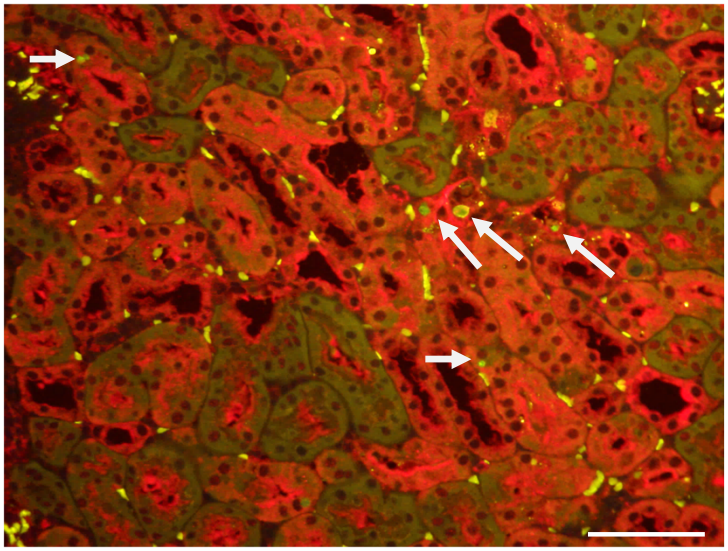

Supplementary Figure 14, Hasegawa et al.

TG＋STZ

TUNEL

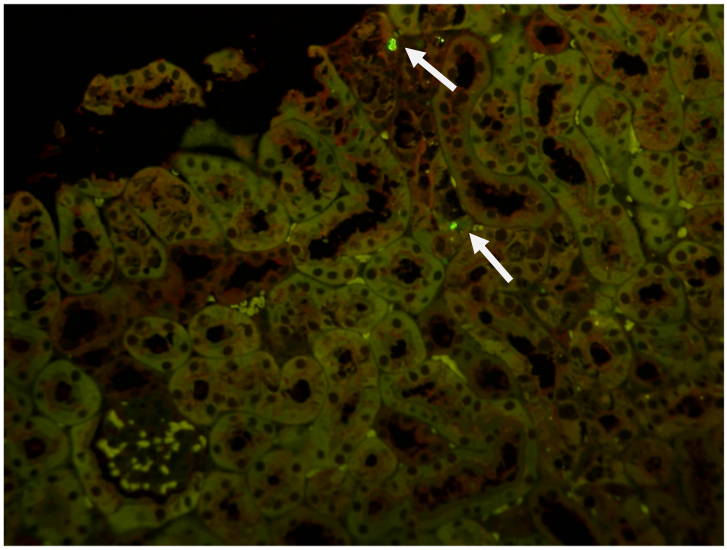

AQP-1

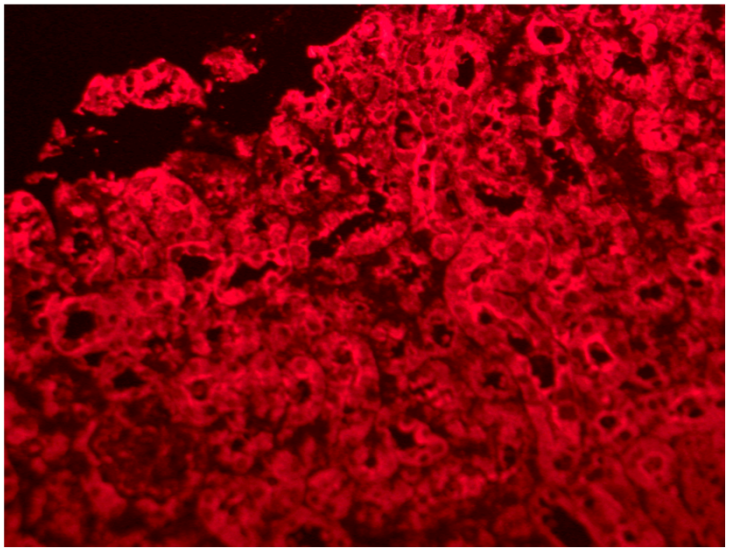

Merged

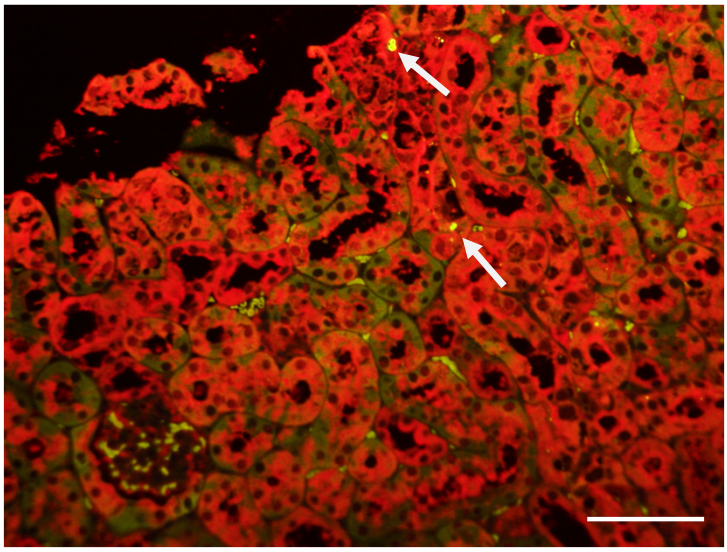

Supplementary Figure 15, Hasegawa et al.

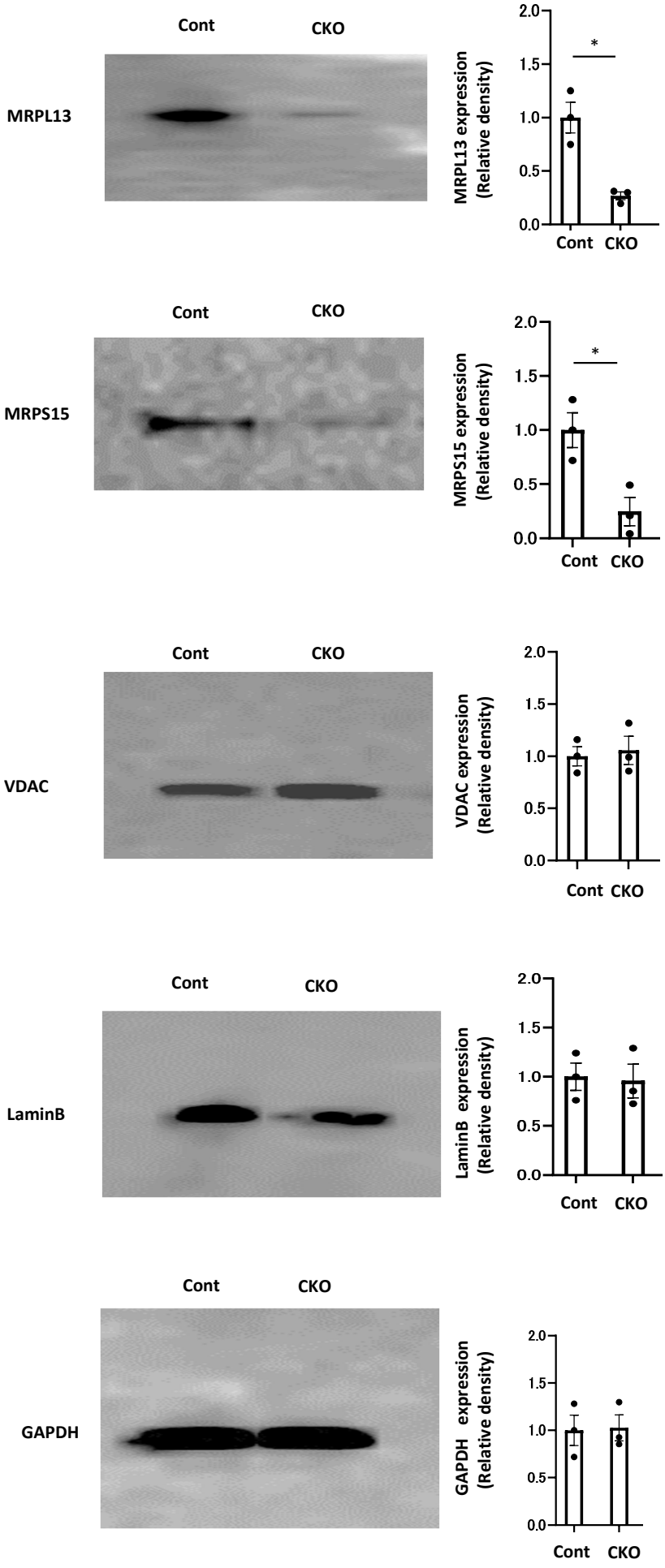

Supplementary Figure 16, Hasegawa et al.

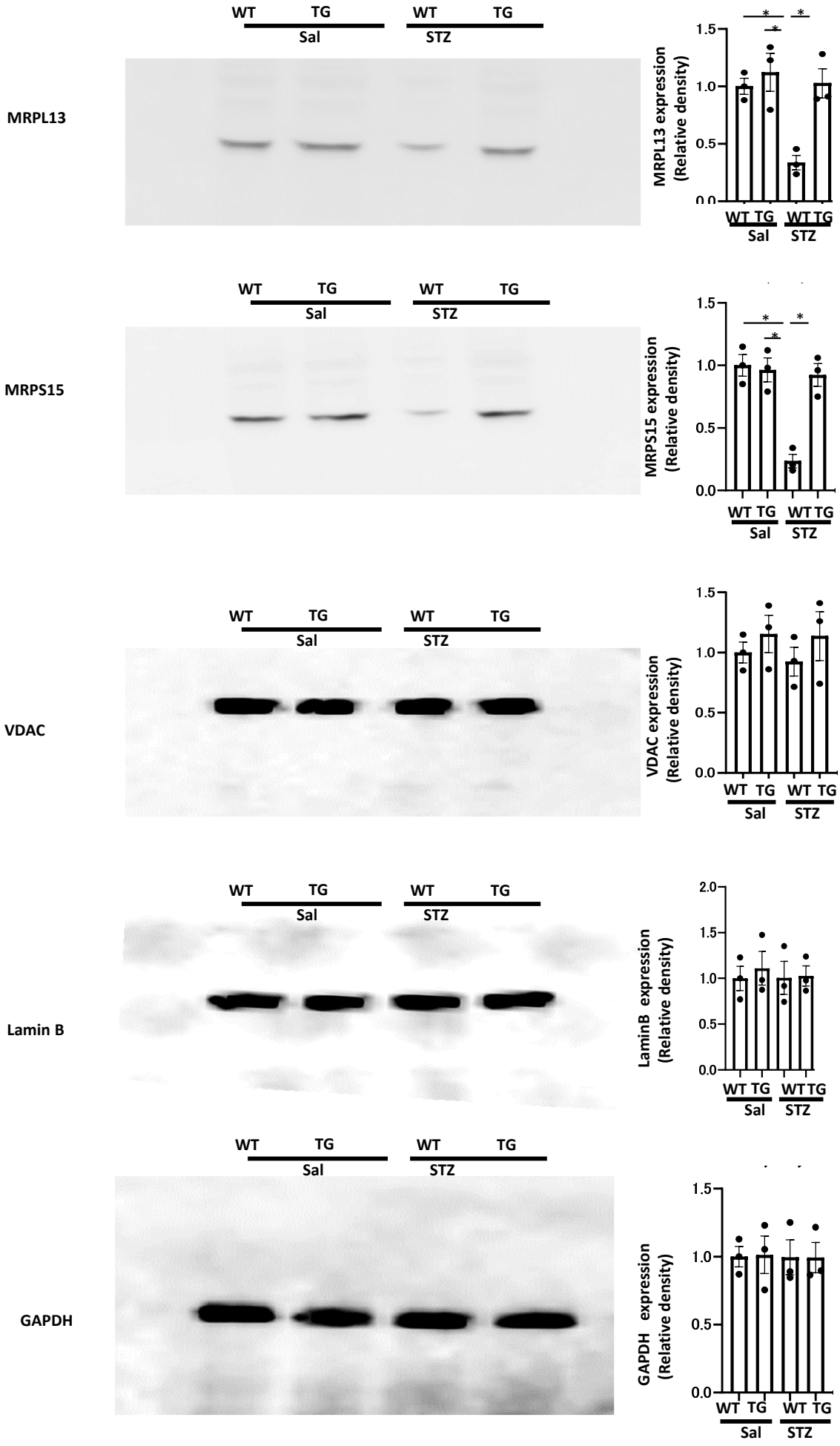

Supplementary Figure 17, Hasegawa et al.

Uncropped blots of MRPL13 in Supplementary Figure 16

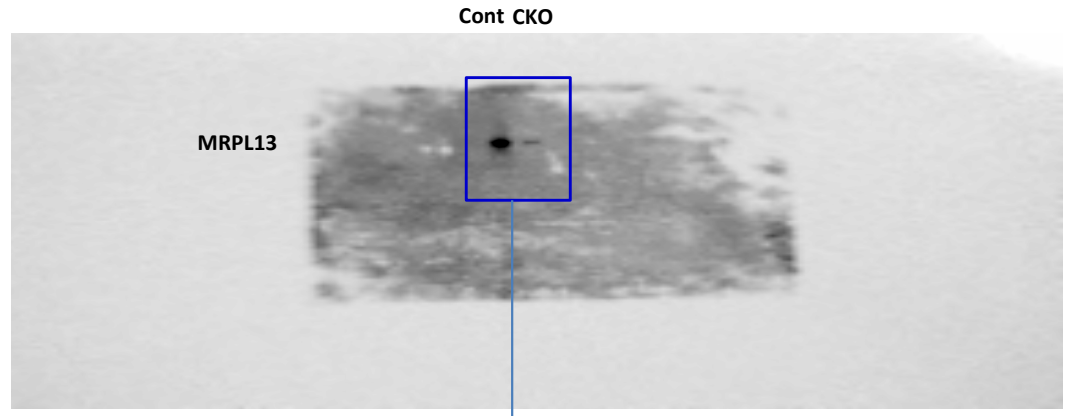

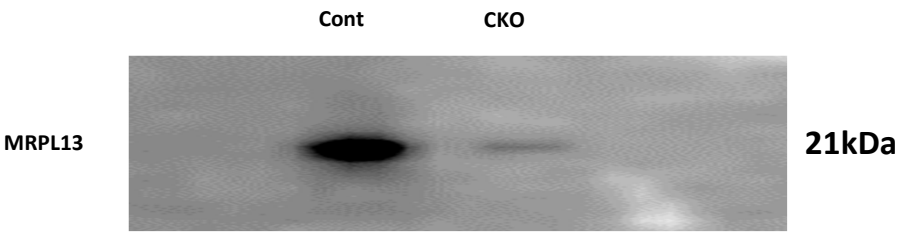

Supplementary Figure 18, Hasegawa et al.

Uncropped blots of MRPS15 in Supplementary Figure 16

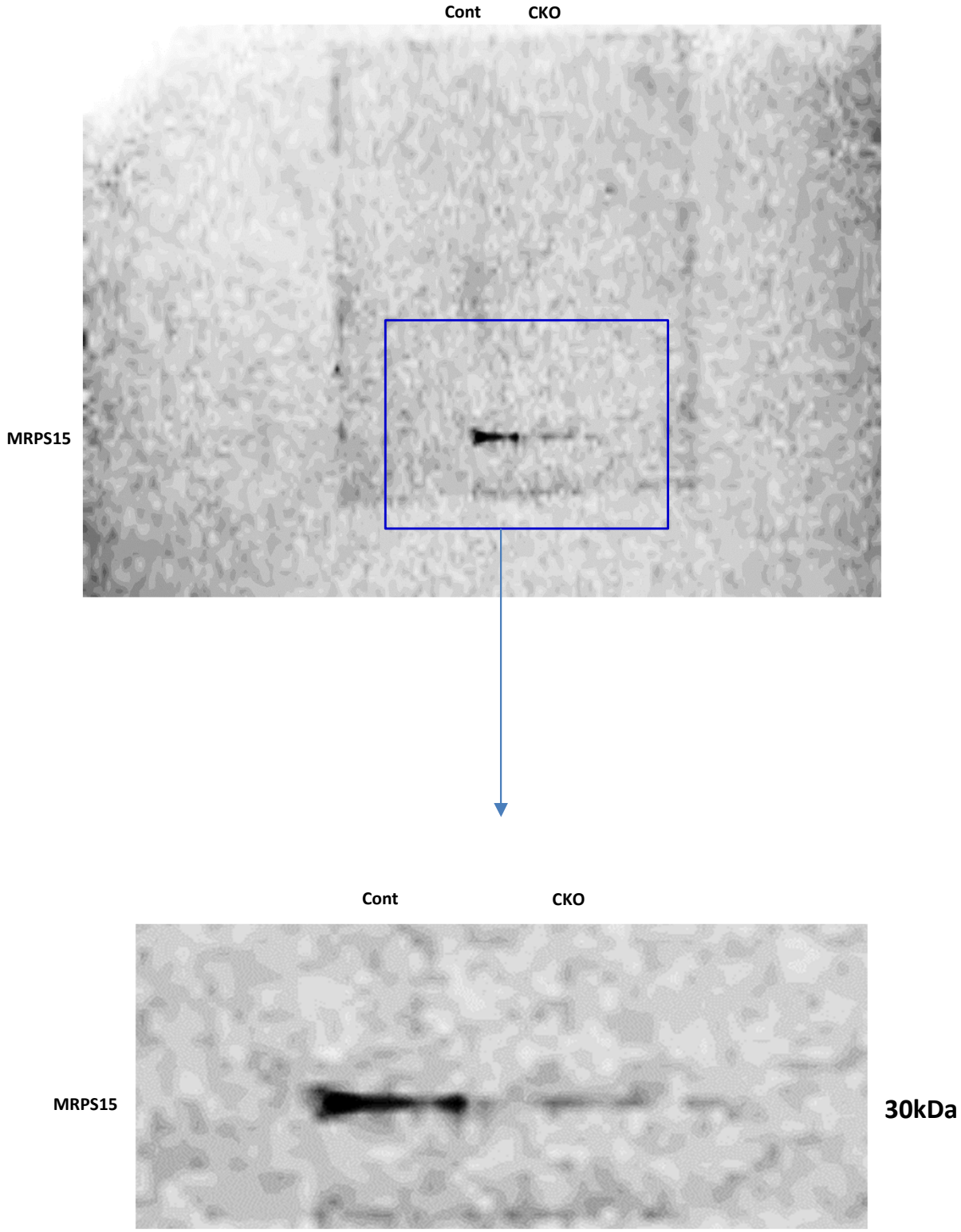

Supplementary Figure 19, Hasegawa et al.

Uncropped blots of VDAC in Supplementary Figure 16

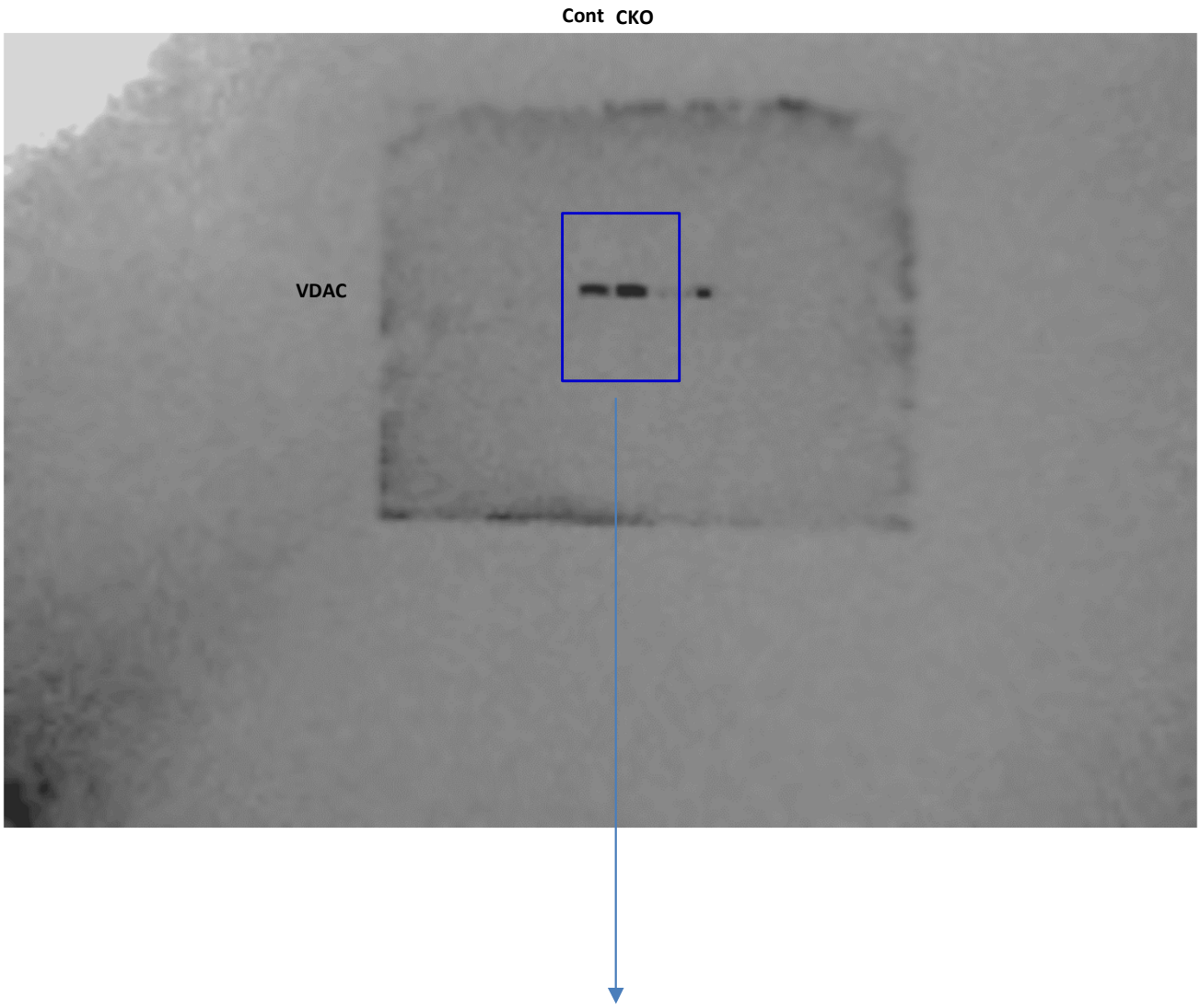

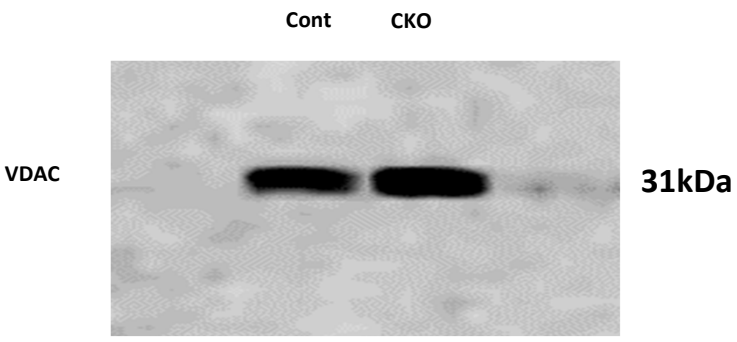

Supplementary Figure 20, Hasegawa et al.

Uncropped blots of Lamin B in Supplementary Figure 16

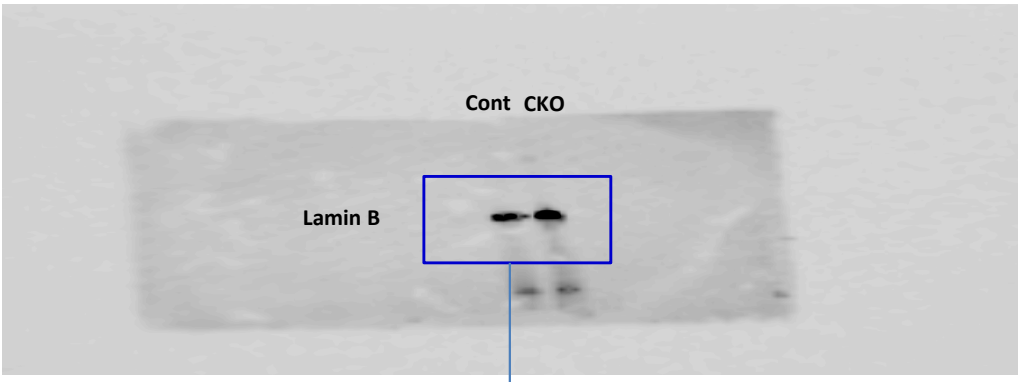

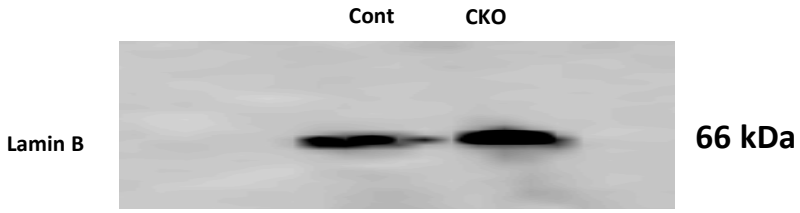

Supplementary Figure 21, Hasegawa et al.

Uncropped blots of GAPDH in Supplementary Figure 16

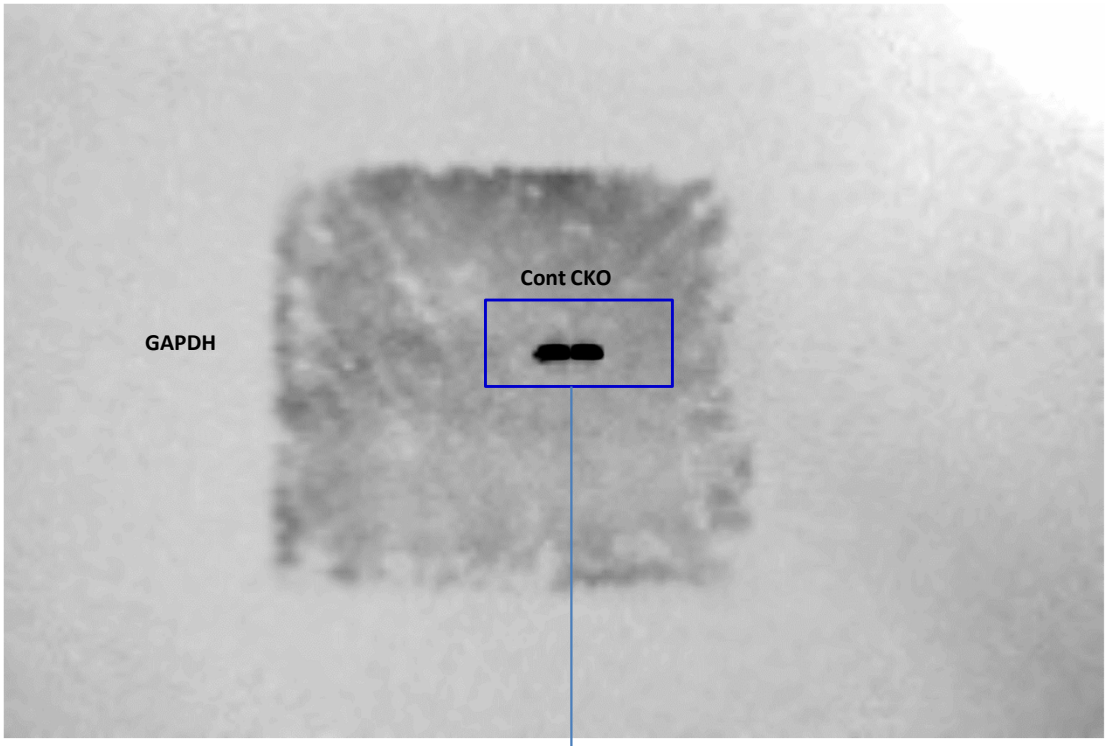

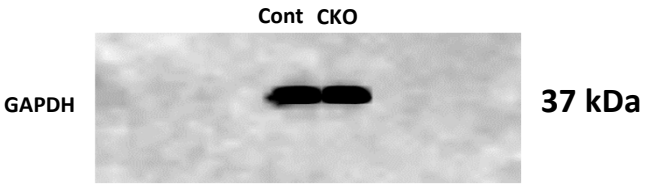

Supplementary Figure 22, Hasegawa et al.

Uncropped blots of MRPL13 in Supplementary Figure 17

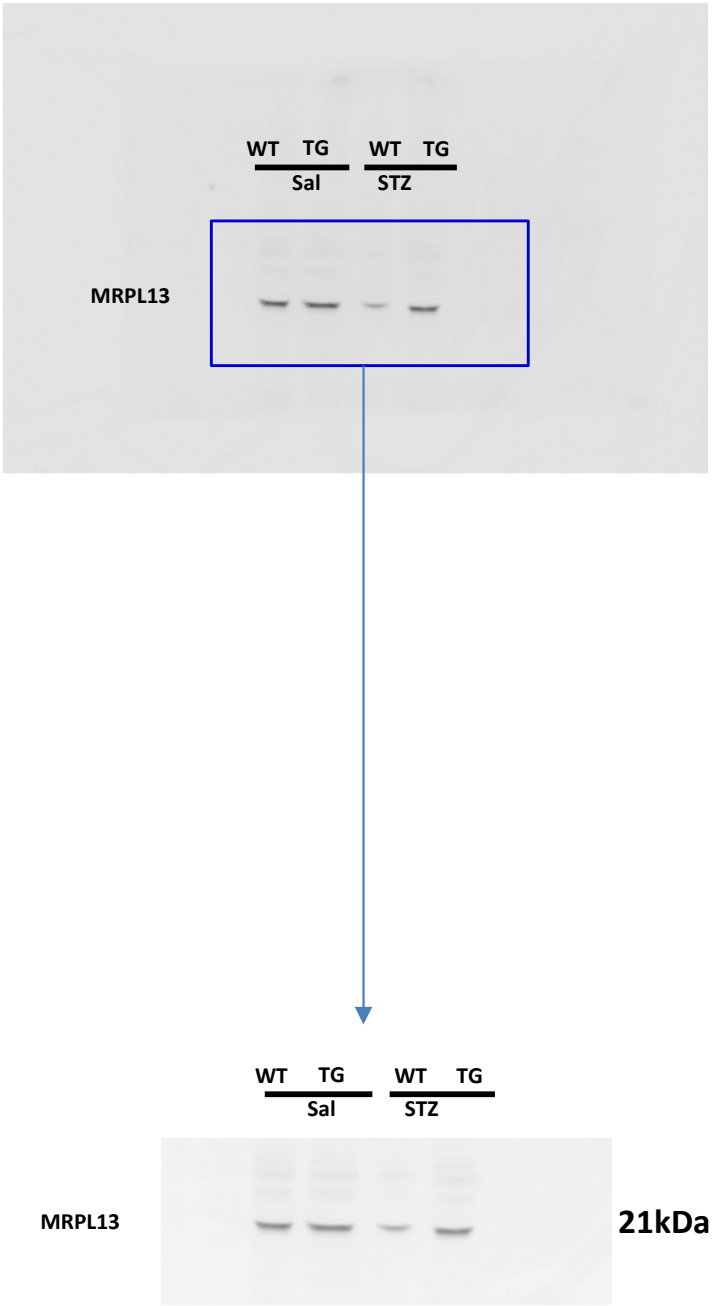

Supplementary Figure 23, Hasegawa et al.

Uncropped blots of MRPS15 in Supplementary Figure 17

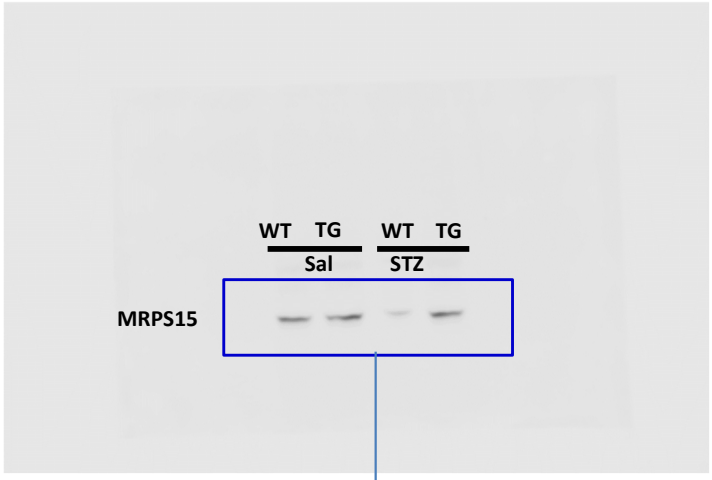

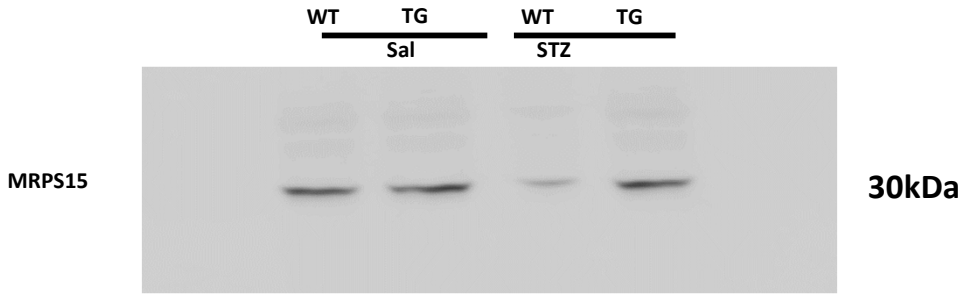

Supplementary Figure 24, Hasegawa et al.

Uncropped blots of VDAC in Supplementary Figure 17

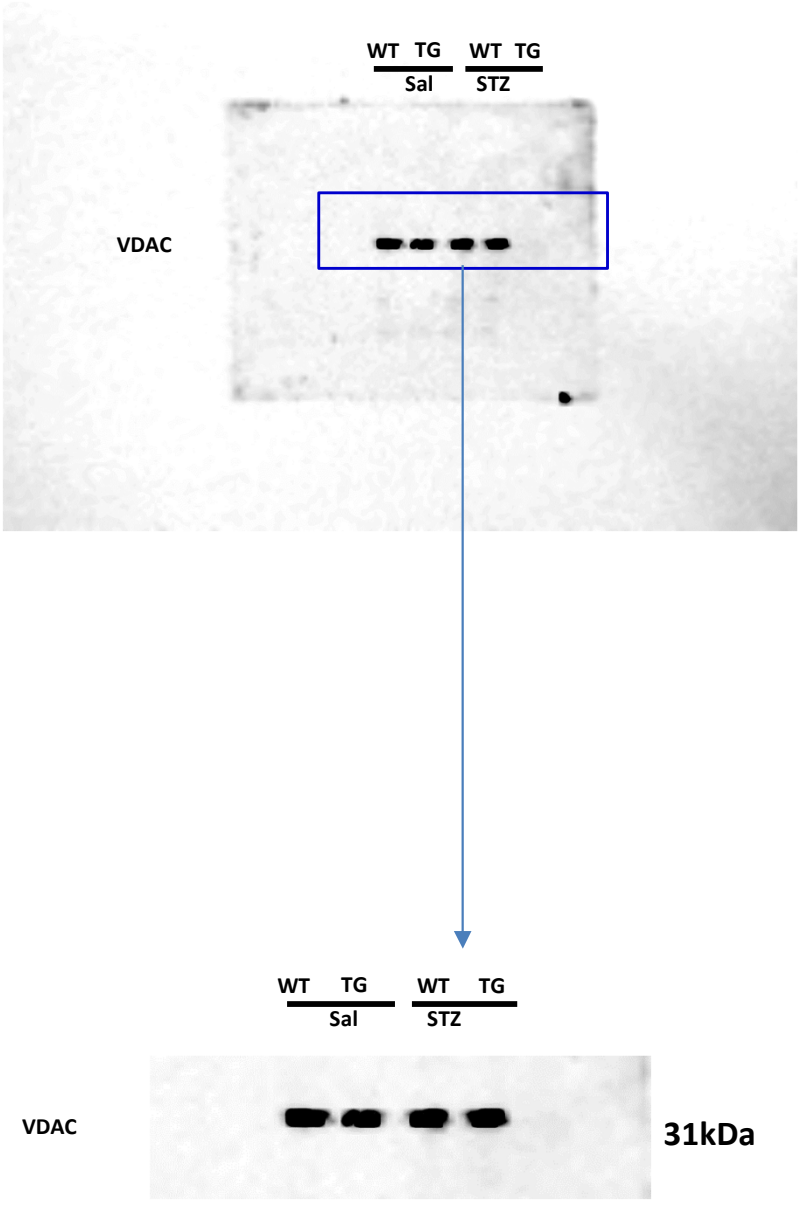

Supplementary Figure 25, Hasegawa et al.

Uncropped blots of Lamin B in Supplementary Figure 17

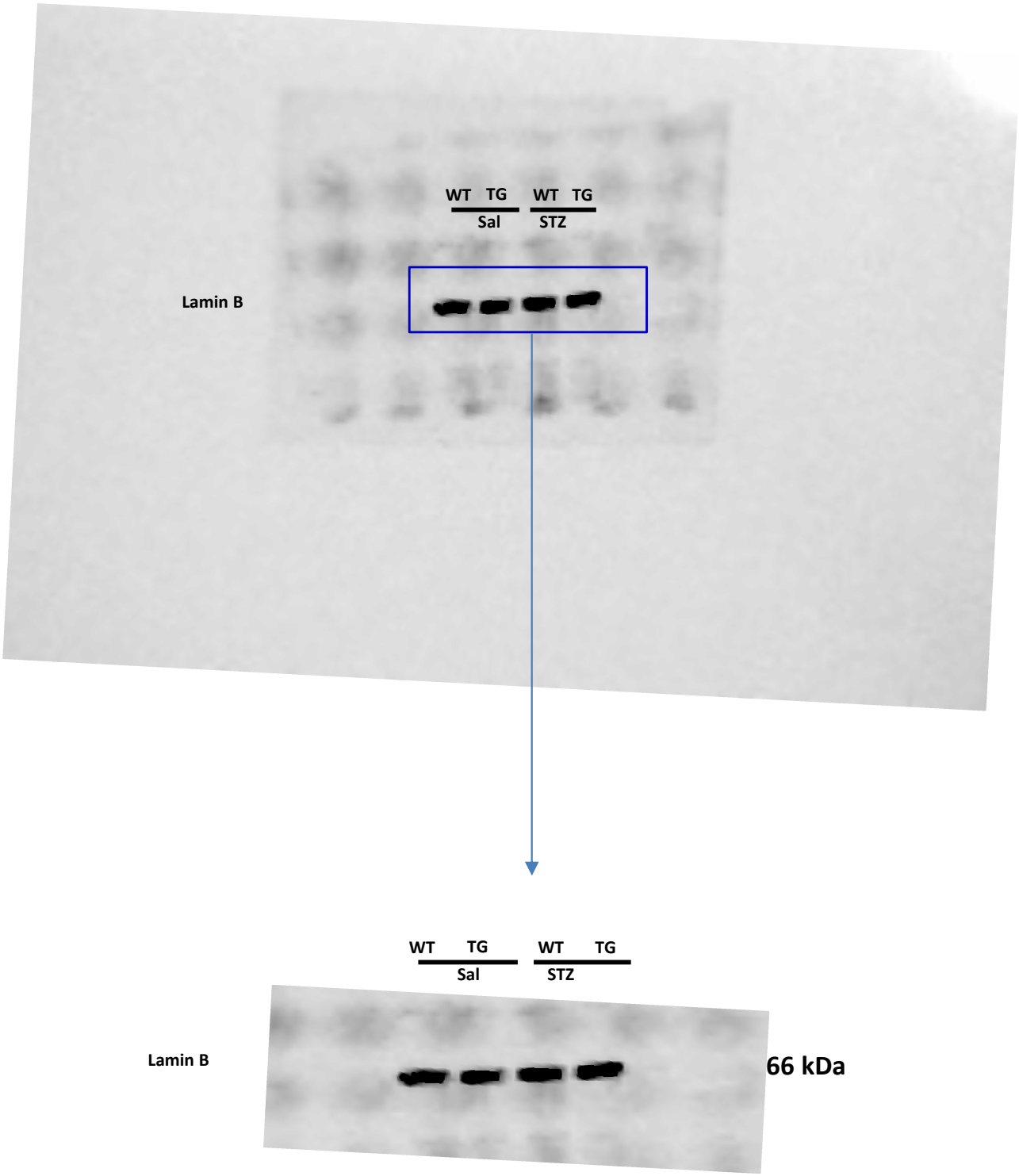

Supplementary Figure 26, Hasegawa et al.

Uncropped blots of GAPDH in Supplementary Figure 17

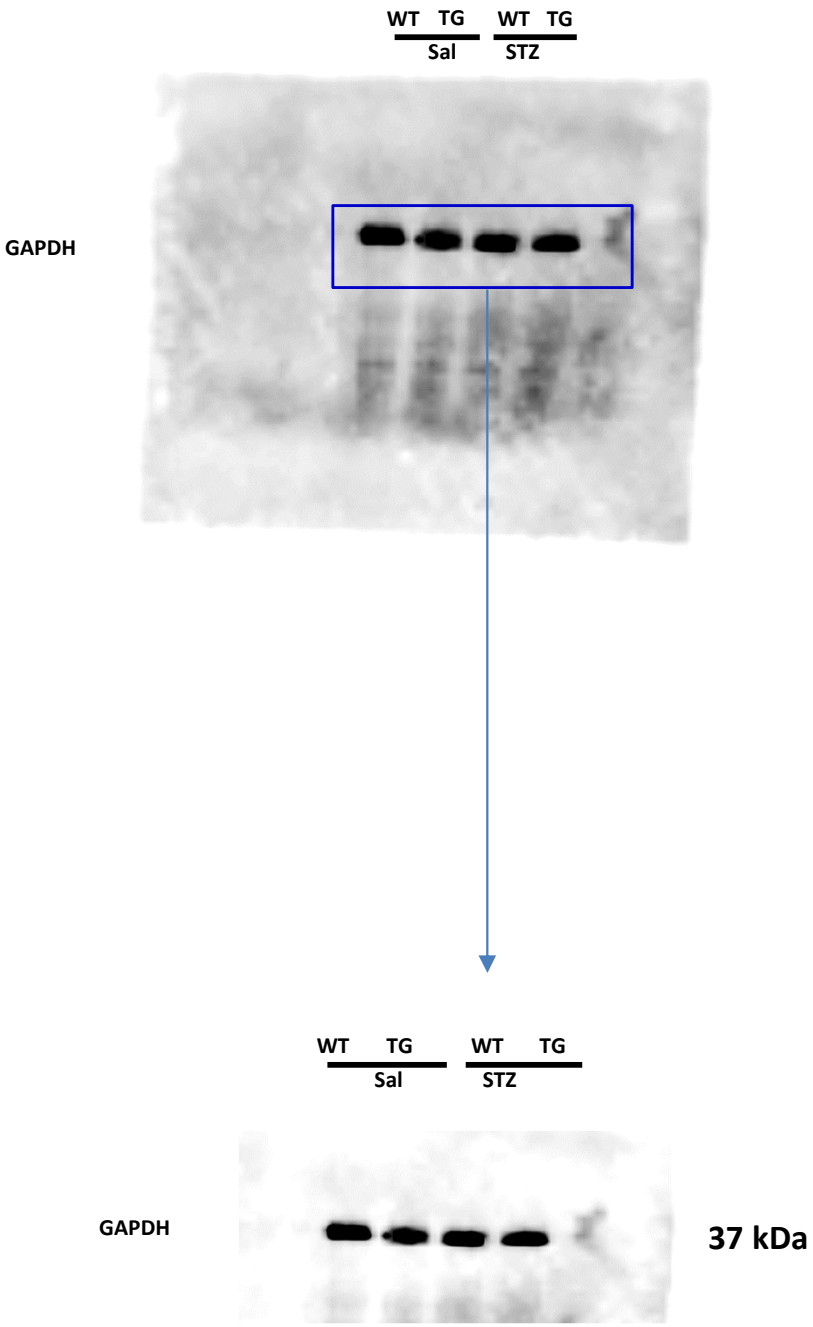

Supplementary Figure 27, Hasegawa et al.

Gene map depicting mit-DNA-encoded genes. These genes are translated in mitoribosomes to produce each protein.

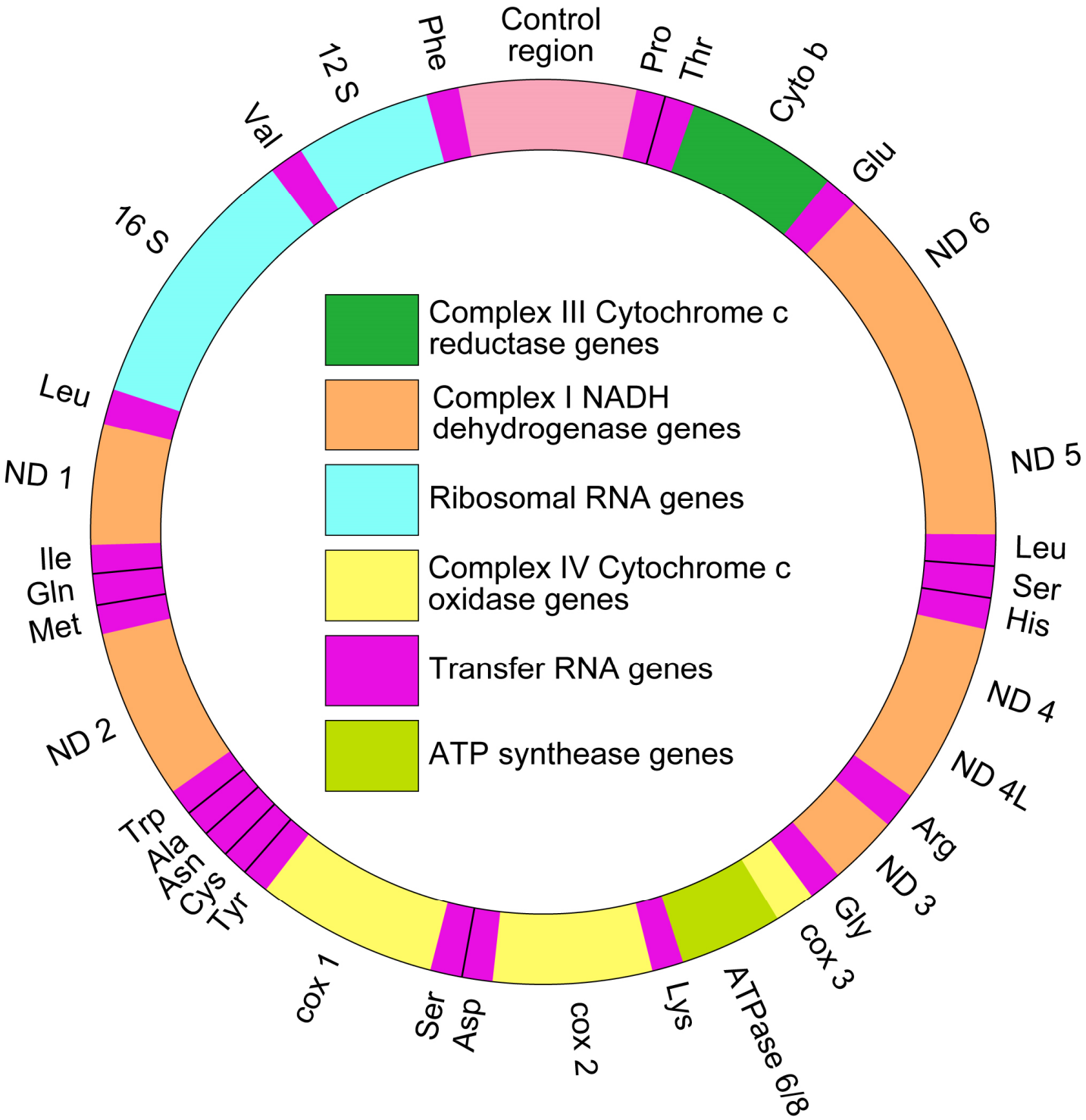

Supplementary Figure 28, Hasegawa et al.

Supplementary References

1. Moore CL, Savenka AV, Basnakian AG: TUNEL Assay: A Powerful Tool for Kidney Injury Evaluation. Int J Mol Sci 22: 412, 2021

2. Muraoka H, Hasegawa K, Sakamaki Y, Minakuchi H, Kawaguchi T, Yasuda I, et al.: Role of Nampt-Sirt6 axis in renal proximal tubules in extracellular matrix deposition in diabetic nephropathy. Cell Rep 27: 199–212.e5, 2019

3. Serna JDC, Amaral AG, Caldeira da Silva CC, Munhoz AC, Vilas-Boas EA, et al.: Regulation of kidney mitochondrial function by caloric restriction. Am J Physiol Renal Physiol 323: F92-F106, 2022

4. Choksi KB, Nuss JE, DeFord JH: Mitochondrial electron transport chain functions in long-lived Ames dwarf mice. J.Aging (Albany NY): 3: 754-67, 2011

5. Gekle M, Knaus P, Nielsen R, Mildenberger S, Freudinger R, Wohlfarth V, et al.: Transforming growth factor-beta1 reduces megalin- and cubilin-mediated endocytosis of albumin in proximal-tubule-derived opossum kidney cells. J Physiol: 552: 471-81, 2003

6. Sa, Y., Li, C., Li, H. and Guo, H: TIMP-1 Induces α-Smooth muscle actin in fibroblasts to promote urethral scar formation. Cell. Physiol. Biochem: 35: 2233–2243, 2015

7. Zelko IN, Zhu J, Roman J: Role of SOD3 in silica-related lung fibrosis and pulmonary vascular remodeling. Respir Res: 19: 221, 2018

8. Koopman WJ, Distelmaier F, Smeitink JA, Willems PH: OXPHOS mutations and neurodegeneration. EMBO J: 32: 9-29, 2013

9. Martínez-Reyes I, Cuezva JM: The H(+)-ATP synthase: a gate to ROS-mediated cell death or cell survival. Biochim Biophys Acta: 1837: 1099-112, 2014

10. Ide T, Tsutsui H, Kinugawa S, Utsumi H, Kang D, Hattori N, et al.: Mitochondrial electron transport complex I is a possible source of oxygen free radicals in the failing myocardium. Circ Res: 85: 357-63, 1999
11. Homma T, Kobayashi S, Sato H, Fujii J: Superoxide produced by mitochondrial complex III plays a pivotal role in the execution of ferroptosis induced by cysteine starvation. Arch Biochem Biophys: 700: 108775, 2021